Molecular mechanism of IgE-mediated FcεRI activation

https://doi.org/10.1038/s41586-024-08229-8

Received: 24 April 2024

Accepted: 16 October 2024

Mengying Chen[1,2,3], **Qiang Su**[1,2,4] ✉ & **Yigong Shi**[1,2,3] ✉

Allergic diseases affect more than a quarter of individuals in industrialized countries, and are a major public health concern[1,2]. The high-affinity Fc receptor for immunoglobulin E (FcεRI), which is mainly present on mast cells and basophils, has a crucial role in allergic diseases[3–5]. Monomeric immunoglobulin E (IgE) binding to FcεRI regulates mast cell survival, differentiation and maturation[6–8]. However, the underlying molecular mechanism remains unclear. Here we demonstrate that prior to IgE binding, FcεRI exists mostly as a homodimer on human mast cell membranes. The structure of human FcεRI confirms the dimeric organization, with each promoter comprising one α subunit, one β subunit and two γ subunits. The transmembrane helices of the α subunits form a layered arrangement with those of the γ and β subunits. The dimeric interface is mediated by a four-helix bundle of the α and γ subunits at the intracellular juxtamembrane region. Cholesterol-like molecules embedded within the transmembrane domain may stabilize the dimeric assembly. Upon IgE binding, the dimeric FcεRI dissociates into two protomers, each of which binds to an IgE molecule. This process elicits transcriptional activation of *Egr1*, *Egr3* and *Ccl2* in rat basophils, which can be attenuated by inhibiting the FcεRI dimer-to-monomer transition. Collectively, our study reveals the mechanism of antigen-independent, IgE-mediated FcεRI activation.

Allergic disorders, exemplified by allergic rhinitis, atopic dermatitis, asthma and food and drug allergies, constitute a mounting healthcare challenge in recent decades[1,2,9]. In these cases, mast cells and basophils are critical effectors[3–5]. These cells express FcεRI, which recognizes soluble IgE. Upon exposure to allergens, IgE-bound FcεRI is crosslinked, which triggers cellular activation and the release of allergic mediators, including histamine, prostaglandins and leukotrienes[6–8]. Immediate allergic reactions are characterized by vasodilation, increased vascular permeability, bronchoconstriction and, in severe cases, systemic anaphylaxis[1,2,4].

FcεRI is a multimeric cell-surface receptor that was discovered in the early 1980s[10,11]. FcεRI belongs to the antigen receptor superfamily, alongside T cell receptors and B cell receptors[6,12]. In human mast cells and basophils, FcεRI consists of one α subunit, one β subunit and two γ subunits[6,7]. In monocytes, Langerhans cells, dendritic cells and eosinophils, FcεRI is expressed as a trimeric $\alpha\gamma_2$ complex[7]. The α subunit has two extracellular immunoglobulin-like domains, which are responsible for binding to the Fc domain of IgE[13,14]. It also has a transmembrane helix and a short cytoplasmic tail without any obvious signalling motif. By contrast, the β and γ subunits, with four and one transmembrane helices respectively, each have an immunoreceptor tyrosine-based activation motif (ITAM) at their carboxyl termini[8].

When FcεRI is engaged by soluble IgE and multivalent antigens, the ITAMs are phosphorylated by the Src family tyrosine kinase LYN. This initiates a rapid signalling cascade, resulting in the release of preformed inflammatory mediators within minutes[15]. In this process, the γ subunits serve as the primary and indispensable signalling components, whereas the β subunit amplifies the signals generated by the γ subunits[16].

IgE was initially thought to be passively attached to FcεRI without influencing mast cell function[17]. However, more recent studies have revealed a number of important IgE-mediated effects on mast cells in the absence of antigens[4,7,18]. For instance, IgE increases FcεRI expression by stabilizing receptors on the cell surface and preventing their internalization[18–20]. Moreover, IgE has a crucial role in promoting mast cell survival[21–23] and activation[24]. The IgE-mediated effects depend on the ITAMs in the γ subunits and utilize a pathway distinct from antigen-dependent signalling[20,25]. Notably, these IgE effects has been validated in various animal models[26,27], underscoring their significance in allergic conditions.

Elevated levels of serum IgE are associated with allergic diseases, and its reduction is beneficial for patients[28–30]. Mechanistic understanding of IgE-mediated effects is pivotal for potential therapeutic intervention. However, the mechanism remains unknown, mainly owing to the lack of structural information on the FcεRI transmembrane domain. In this study, we report the full-length FcεRI structure at 3.8 Å resolution using cryo-electron microscopy (cryo-EM). Through experimental analyses, we identified a functionally important FcεRI dimer-to-monomer transition upon IgE binding. This transition initiates downstream signalling that may contribute to mast cell and basophil survival and activation.

---

[1]Research Center for Industries of the Future, Key Laboratory of Structural Biology of Zhejiang Province, School of Life Sciences, Westlake University, Institute of Biology, Westlake Institute for Advanced Study, Hangzhou, China. [2]Westlake Laboratory of Life Sciences and Biomedicine, Hangzhou, China. [3]Beijing Advanced Innovation Center for Structural Biology, Tsinghua-Peking Joint Center for Life Sciences, School of Life Sciences, School of Medicine, Tsinghua University, Beijing, China. [4]Present address: Institute of Bio-Architecture and Bio-Interactions (IBABI), Shenzhen Medical Academy of Research and Translation (SMART), Shenzhen, China. ✉e-mail: suqiang@smart.org.cn; syg@westlake.edu.cn

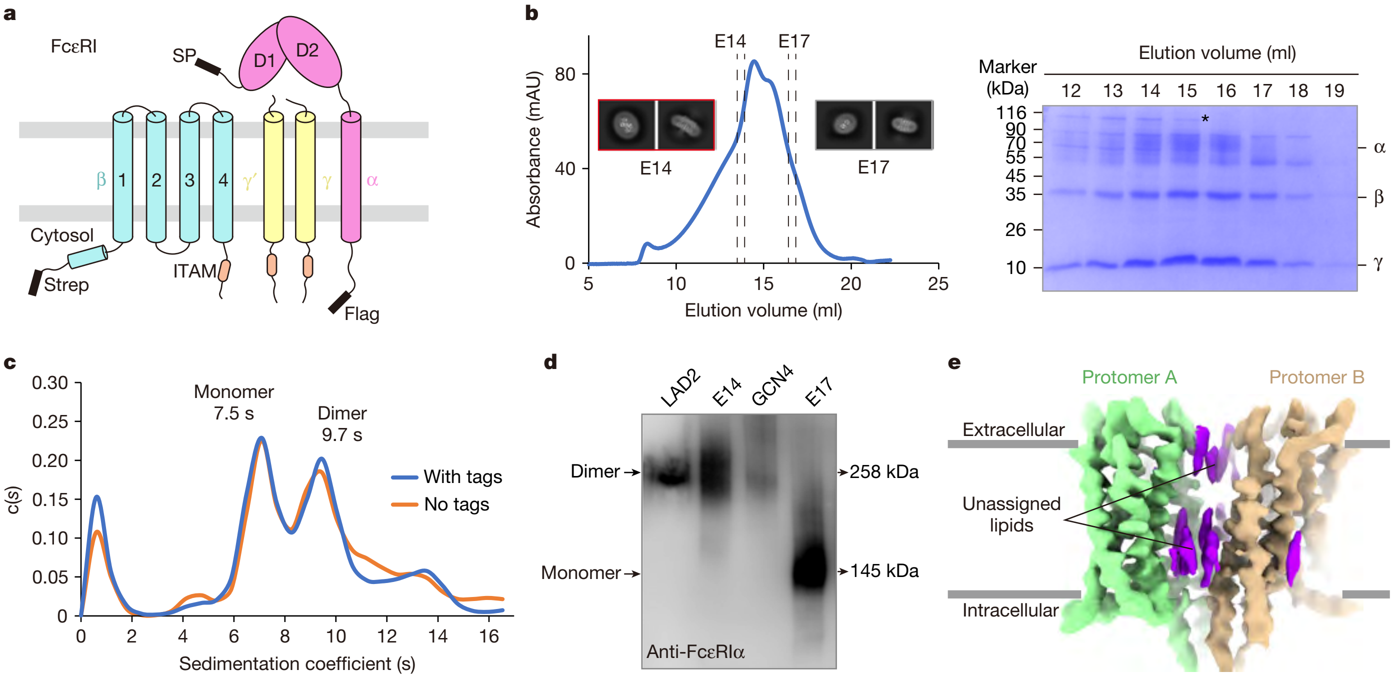

Fig. 1 | Biochemical and cryo-EM analysis of human FcεRI. a, A schematic diagram of the FcεRI protomer used in our studies. Each FcεRI protomer has four subunits, with one α, one β and two γ subunits ($\alpha\beta\gamma_2$). The C and N termini of the α and β subunits are fused to Flag and Strep tags, respectively. D1 and D2 are two immunoglobulin-like domains of the α subunit. SP, signal peptide. **b**, Left, chromatogram showing purification of human FcεRI by SEC. Inset: The fractions E14 and E17, bracketed by dashed lines, contain human FcεRI in its dimeric and monomeric forms, respectively. Samples from these two fractions were analysed by cryo-EM. Images show representative 2D class averages of dimeric (E14) and monomeric (E17) FcεRI. Right, peak fractions from the SEC were visualized by SDS–PAGE with Coomassie staining. The bands were analysed by mass spectrometry; these results are presented in Source Data. The asterisk indicates the position of calnexin bands. Results are representative of two independent experiments. **c**, AUC analysis of human FcεRI with and without affinity tags. The two peaks of sedimentation coefficients—7.5 s and 9.7 s—correspond to the molecular masses of monomeric and dimeric FcεRI, respectively. c(*s*), sedimentation coefficient. **d**, Native gel analysis of FcεRI from LAD2 cells, FcεRI from E14 and E17 fractions (**b**) and GCN4–FcεRI shows that human FcεRI exists mostly as homodimers in LAD2 cells. Results are representative of three independent experiments. Molecular mass markers are indicated by AUC results. **e**, The overall cryo-EM map (contoured at 6σ) of human FcεRI. FcεRI exists as a stable homodimer. Unassigned lipids are shown in purple.

Biochemical characterization of FcεRI

To facilitate protein purification, we fused affinity tags to the carboxyl and amino termini of the α and β subunits of FcεRI (Fig. 1a). The recombinant FcεRI was purified using tandem affinity purification and size-exclusion chromatography (SEC) (Fig. 1b). The SEC profile shows a polydisperse peak, indicative of heterogeneity within the purified FcεRI complex. The heterogeneity was confirmed through analytical ultracentrifugation (AUC), which revealed two distinct peaks with sedimentation coefficients of 7.5 s and 9.7 s (Fig. 1c). To eliminate potential influence of the affinity tags on FcεRI oligomerization, we removed the tags using the DrICE protease[31]. The AUC profile of the tag-free FcεRI was very similar to that of the tagged version.

We performed cryo-EM analysis on two SEC elution fractions, E14 and E17 (Fig. 1b). On the basis of representative two-dimensional (2D) averages, the molecular mass in E14 was markedly larger than that in E17 (Fig. 1b, inset). Notably, the protein in E14 appears to contain twice the number of transmembrane helices of the one in E17. This observation suggests that the dominant form of FcεRI is likely to be dimeric ($\alpha_2\beta_2\gamma_4$) in E14 and monomeric ($\alpha\beta\gamma_2$) in E17.

We overexpressed the recombinant FcεRI in mammalian cells, but the oligomeric state of endogenous FcεRI in mast cells remained unclear. Therefore, we assessed endogenous FcεRI from the human mast cell line LAD2[32] using blue native polyacrylamide gel electrophoresis (BN-PAGE). Consistent with cryo-EM analysis, recombinant FcεRI from E14 and E17 resolved into two distinct positions that correspond to the molecular masses of the dimeric and monomeric forms of FcεRI, respectively (Fig. 1d, lanes 2 and 4). We also confirmed the results by using a constitutive dimer of FcεRI (GCN4–FcεRI), with a leucine zipper GCN4[33] fused to the carboxyl terminus of the α subunit (Fig. 1d, lane 3). Most notably, endogenous FcεRI from LAD2 cells resolved to a single position that corresponds to the dimeric form of FcεRI, as shown by E14 and GCN4–FcεRI (Fig. 1d, lane 1). These results suggest that endogenous FcεRI in mast cells exists mostly in the dimeric form prior to IgE binding.

The structure of FcεRI

Next, we embarked on structure determination. FcεRI is a challenging target for cryo-EM analysis owing to the lack of an ordered extracellular domain. We mounted a rigorous effort of sample preparation and data processing over several years (see Methods for details). Eventually, we obtained a cryo-EM reconstruction of the dimeric FcεRI at an average resolution of 3.8 Å (Extended Data Figs. 1 and 2 and Extended Data Table 1).

FcεRI is indeed a symmetric homodimer, with two protomers stacking against each other mostly through their respective transmembrane helices from the α subunits (Fig. 1e). A number of unassigned lipid molecules are nestled within the cleft between the two protomers, probably enhancing their association (Fig. 1e). With the assistance of AlphaFold2 multimer[34], we built an atomic model for this complex (Fig. 2a and Extended Data Fig. 3a). The extracellular domains of the α subunits (ECDα) have little electron microscopy density, suggesting a flexible linkage to the transmembrane domain. The transmembrane domain exhibits a layered organization, with two transmembrane helices from the α subunits at the centre, which are encapsulated

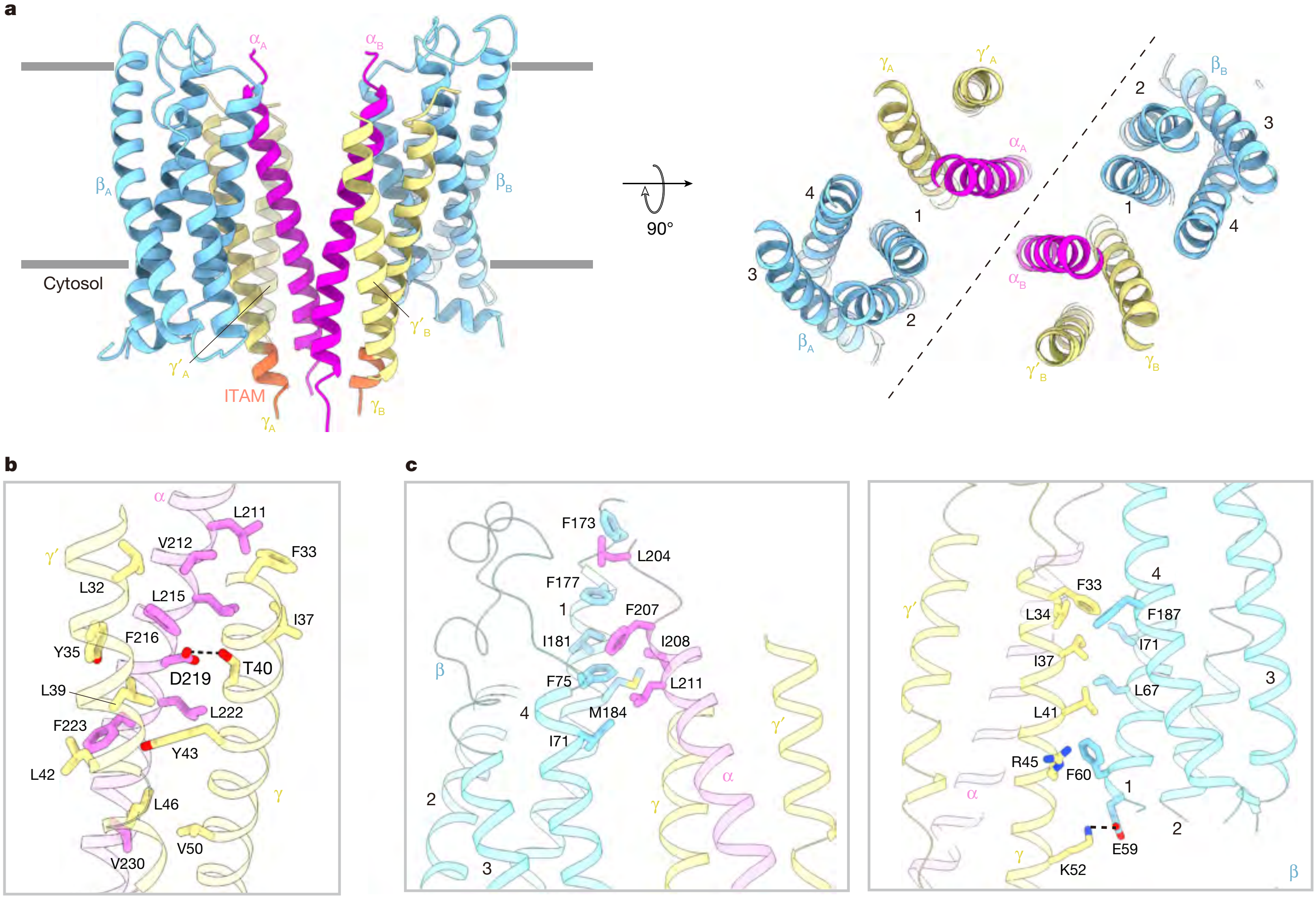

Fig. 2 | Structure of human FcεRI. a, Atomic structure of human FcεRI in its dimeric state. Two perpendicular views are shown. The FcεRI dimer contains two α subunits (magenta), two β subunits (cyan) and four γ subunits (pale yellow). The ITAM motifs on the γ subunits are shown in orange. The colour scheme used in this panel is maintained throughout this Article. **b**, A close-up view on the interface between the α subunit and the two γ subunits. Hydrogen bonds are indicated by black dashed lines. **c**, Two close-up views on the interfaces involving the β subunit: interfaces between the β and α subunits (left) and interfaces between the β and γ subunits (right). Hydrogen bonds are indicated by black dashed lines. Structural figures were prepared using UCSF ChimeraX[51] unless otherwise indicated.

by four transmembrane helices from the γ subunits (Fig. 2a). Within each protomer, two transmembrane helices, one each from the α and γ subunits, stack against a transmembrane four-helix bundle from the β subunit.

In each protomer, the transmembrane helix of the α subunit (TMα) interacts with two transmembrane helices of the γ subunits (TMγ and TMγ′) through extensive van der Waals contacts, mostly involving bulky residues (Fig. 2b). Notably, Asp219 in TMα accepts a hydrogen bond from Thr40 in TMγ. At the interface between the α and γ subunits and the β subunit, four hydrophobic residues (Leu204, Phe207, Ile208 and Leu211) at the N-terminal portion of TMα contact a greasy surface formed by TMβ1 and TMβ4 near the extracellular side (Fig. 2c, left). TMγ aligns with TMβ1 and TMβ4, establishing extensive interactions. In particular, Arg45 and Lys52 in TMγ form a cation–π interaction and a hydrogen bond with Phe60 and Glu59 in TMβ1, respectively (Fig. 2c, right). At the current resolution, these interactions are assigned on the basis of the tentatively modelled residues.

In contrast to the transmembrane domains of T and B cell receptors, which contain many buried hydrogen bonds[35,36], the assembly of the transmembrane domain in FcεRI is predominantly governed by van der Waals interactions. With a reduced number of hydrogen bonds to maintain the register of transmembrane helices, the transmembrane domain of FcεRI may be more susceptible to conformational changes upon engagement by IgE and antigens.

The dimeric interface of FcεRI

The dimeric interface of FcεRI is mediated by the juxtamembrane helices of the α and γ subunits on the intracellular side (Figs. 2a and 3a). Specifically, two TMα helices and two TMγ helices form a four-helix bundle (Fig. 3a). At the dimeric interface, Gln228 from TMα of one protomer makes a hydrogen bond to Gln229 from TMα of the other protomer (Fig. 3b, top and Extended Data Fig. 3b). This interface also involves extensive van der Waals contact, exemplified by two closely positioned Phe232 residues at the centre (Fig. 3b, bottom and Extended Data Fig. 3c).

To corroborate our structural findings, we generated three FcεRI variants, which have three residues—Gln228, Gln229, Phe232—of the α subunit replaced by Ala228, Ala229 and Ala232, Glu228, Glu229 and Ala232, or Arg228, Arg229 and Arg232. Next, we used AUC to assess the monomer-to-dimer ratio of FcεRI after affinity purification. Compared with the wild-type FcεRI, the monomer-to-dimer ratio was markedly increased in each of the three FcεRI variants (Fig. 3c and Extended Data Fig. 3d). Presumably, the aggregate mutations weaken the dimeric interface of FcεRI, facilitating the dimer-to-monomer transition.

In our structure, approximately one-quarter of the ITAM sequences (AITSYEKS) are clearly present at the C-terminal helices of TMγ_A and TMγ_B, but absent in TMγ'_A and TMγ'_B (Figs. 2a and 3a and Supplementary Fig. 3. In the dimeric FcεRI, all four ITAM motifs are positioned close

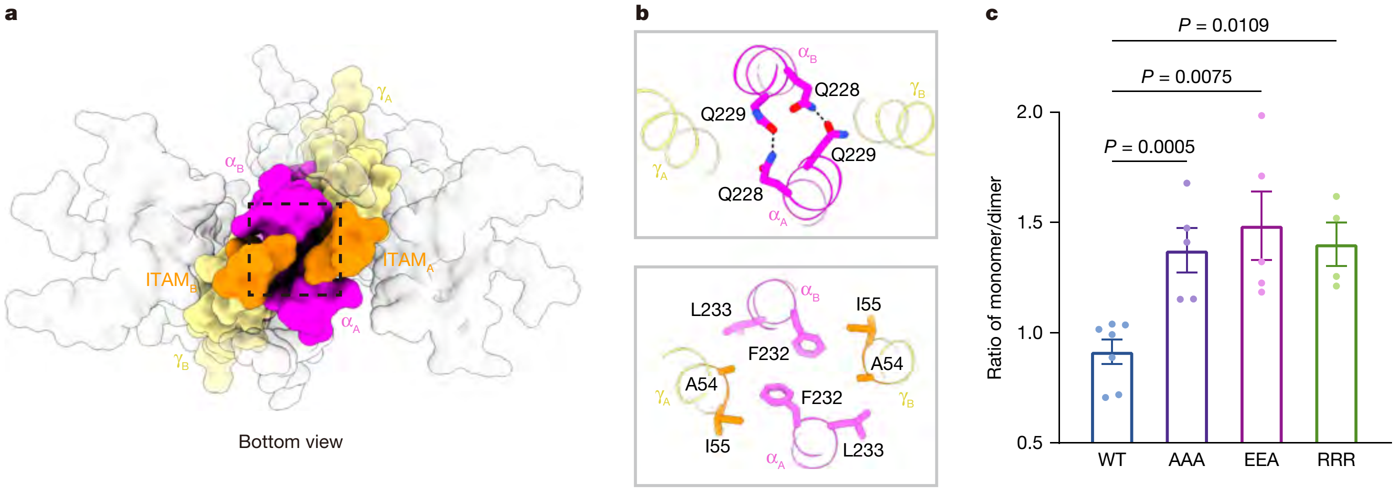

Fig. 3 | The dimer interface of human FcεRI on the intracellular juxtamembrane region. a, The dimer interface of human FcεRI, involving a four-helix bundle, is formed by two transmembrane helices of the α subunits (magenta) and two transmembrane helices of the γ subunits (pale yellow) on their intracellular side. The ITAMs (orange) on the γ subunits are shielded by the transmembrane helices of the α subunits. The β and γ′ subunits are transparent for clarity. **b**, Two close-up views on the interface within the four-helix bundle. Hydrogen bonds are indicated by black dashed lines. **c**, Destabilizing mutations at the dimer interface result in increased ratios of monomer/dimer. The mutations are introduced in α subunits. AAA, Q228A/Q229A/F232A; EEA, Q228E/Q229E/F232A; RRR, Q228R/Q229R/F232R. Data are mean ± s.e.m. Dots correspond to independent experiments (wild type (WT), $n = 7$; AAA, $n = 5$; EEA, $n = 4$; RRR, $n = 4$). Two-sided paired Student's *t*-test.

to each other—in particular ITAMγ_A and ITAMγ_B, which are partially shielded by TMα_A and TMα_B (Fig. 3a). Previous studies suggest that kinases may bind to the extended loop of the ITAM motifs[37]. The close proximity of the ITAM motifs in the dimeric FcεRI might hinder their association with downstream kinases owing to steric hindrance.

Cholesterol may stabilize dimeric FcεRI

In addition to the juxtamembrane helices on the intracellular side, the dimerization of FcεRI is mediated by lipid molecules within the transmembrane domain (Fig. 1e). We scrutinized the electron microscopy densities and inferred that some of them might correspond to cholesterol-like molecules on the basis of their shape at different contour levels (Extended Data Fig. 4a). In each protomer, the cholesterol-like molecule is embedded in a cleft formed by TM1 and TM2 of the β chain and the transmembrane helices of the α and γ chains. To test this binding cleft, we introduced several tryptophan mutations around the lipid-binding site in FcεRI and assessed the cholesterol content of these mutants using mass spectrometry (Extended Data Fig. 4b). We identified three mutants: (1) I224W in the α chain and V38W in the γ chain; (2) V63W in the β chain; and (3) G221W and I224W in the α chain—that exhibited significantly reduced cholesterol content compared with wild-type FcεRI (Extended Data Fig. 4b). These data suggest that the lipid densities within the transmembrane domains may correspond to cholesterol.

Next, we used AUC to analyse the oligomerization state of these FcεRI mutants. Remarkably, all of these mutants exhibited a single peak with sedimentation coefficients of 7.4 s, 8.2 s and 7.2 s, respectively, corresponding to the molecular mass of monomeric FcεRI (Extended Data Fig. 4c). The peak corresponding to the dimer was nearly diminished in these mutants, indicating a tendency toward monomer formation. Together with the structural findings, we speculate that cholesterol molecules embedded in the transmembrane domain may stabilize the dimeric state of FcεRI.

IgE binding induces dimer-to-monomer transition

Because the organization of FcεRI in its dimeric state appears to be unfavourable to downstream kinase signalling, we suspected a transition to another state upon IgE binding. To examine this possibility, we incubated an excess amount of IgE with the dimeric FcεRI to form a distinct IgE–FcεRI complex (Extended Data Fig. 5a). Using this sample, we prepared cryo-EM grids and collected micrographs. Following our standard protocol of data processing, we determined the structure of the IgE–FcεRI complex at an average resolution of 3.19 Å (Extended Data Figs. 5b–f and 6). We built an atomic model with the help of AlphaFold2[34] (Extended Data Fig. 7). As anticipated, the IgE-bound FcεRI exists as a monomer, in which ECDα is stabilized by the Fcε domain of IgE[13] (Fig. 4a and Extended Data Fig. 8). Notably, in our IgE–FcεRI structure, the entire Fc domain and the Cε1 and Cλ regions of both Fab domains are resolved (Extended Data Fig. 7d).

Modelling studies suggest that upon IgE binding, the dimeric FcεRI would dissociate into two monomers owing to steric hindrance between the two IgE–ECDα complexes (Fig. 4b). In apo FcεRI, the two ECDα domains are invisible, indicating considerable conformational flexibility. IgE binding stabilizes and imposes a specific conformation and position for the ECDα, which leads to steric clashes between the two ECDα. Consequently, the dimeric FcεRI dissociates into monomers, with each ECDα binding to one IgE molecule.

To further examine the dimer-to-monomer transition, we assessed the oligomeric state of FcεRI using ultracentrifugation analysis (Fig. 4c). First, we determined the sedimentation coefficient and molecular mass for the monomeric wild-type FcεRI (7.5 s and 145 kDa), the dimeric wild-type FcεRI (9.8 s and 258 kDa), GCN4–FcεRI (9.5 s and 272 kDa) and IgE (7.8 s and 195 kDa) (Fig. 4c). Next, we incubated a stoichiometric amount of IgE with each of the three forms of FcεRI. Notably, the sedimentation coefficient and molecular mass of the monomeric wild-type FcεRI bound to IgE (10.5 s and 345 kDa) are very similar to those of the dimeric wild-type FcεRI bound to IgE (10.8 s and 347 kDa) (Fig. 4c). This result strongly suggests dissociation of the wild-type FcεRI dimer into two monomers upon IgE binding. In addition, the observed molecular mass of the IgE–wild-type FcεRI complex is very close to that of a 1:1 complex between a FcεRI monomer and an IgE (145 kDa + 195 kDa = 340 kDa). Consistent with this analysis, the constitutively dimeric GCN4–FcεRI, which cannot dissociate into monomers upon binding to IgE, exhibited a larger sedimentation coefficient and molecular mass (15.0 s and 484 kDa) (Fig. 4c). The molecular mass of the IgE–GCN4–FcεRI complex is very close to that of a 2:1 complex between

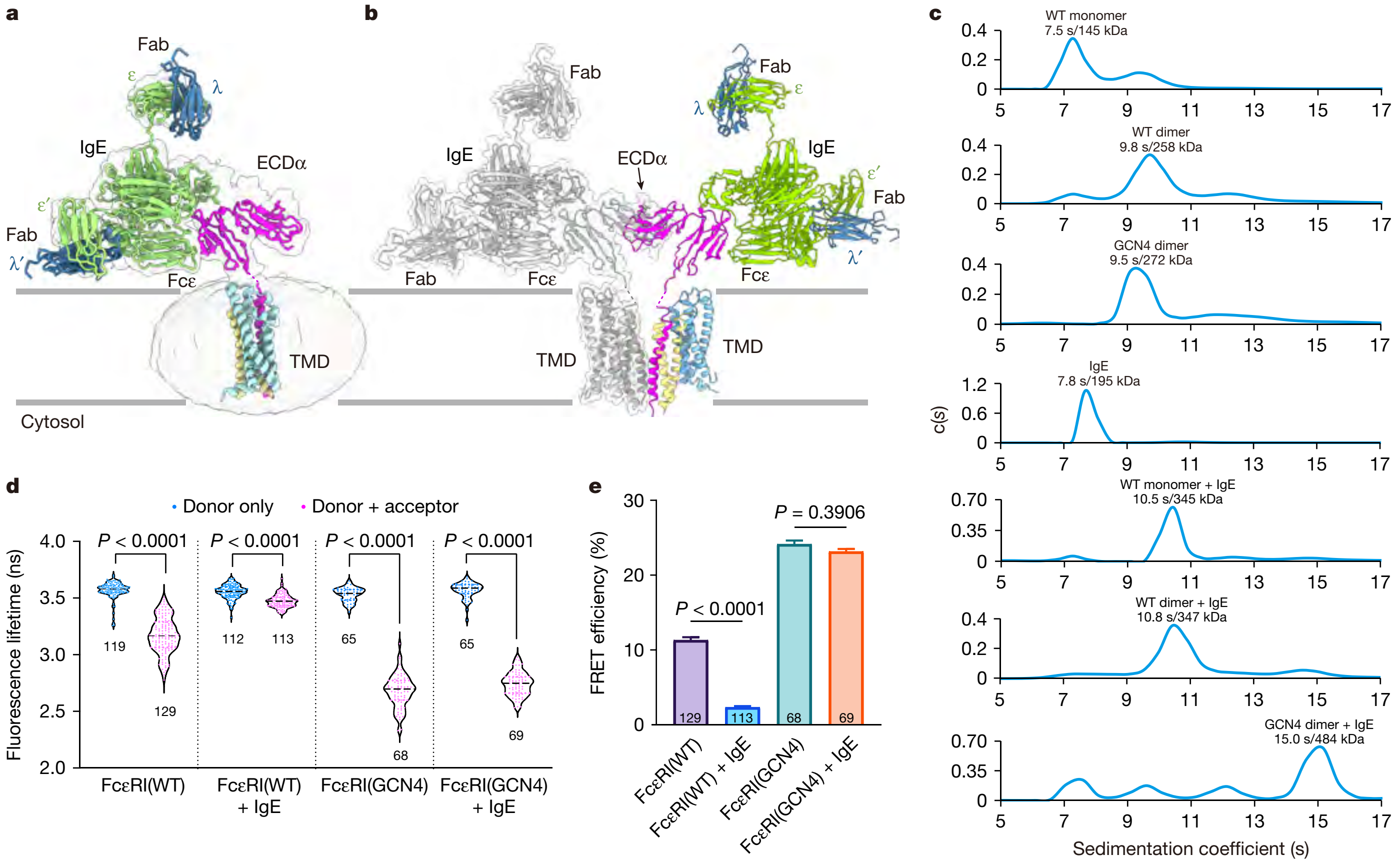

Fig. 4 | Human FcεRI undergoes a dimer-to-monomer transition upon IgE engagement. a, Structure of human FcεRI bound to IgE. The atomic model of FcεRI predicted by AlphaFold2[34] is docked into the electron microscopy map (contoured at 2σ). The ε and λ chains of IgE are shown in green and blue, respectively. TMD, transmembrane domain. **b**, Human FcεRI in its dimeric state is unable to engage two IgE molecules. Shown here is a docking model of two IgE molecules onto FcεRI in its dimeric state. One IgE–FcεRI complex is shown in transparent surface. Severe steric clashes are seen between the two ECDα domains. **c**, Results of AUC analysis on various forms of FcεRI and their complexes with IgE. IgE binding triggers dissociation of the FcεRI dimer into two monomers. Results are representative of three independent experiments. **d**, FRET signals are inhibited by IgE binding for wild-type FcεRI, but not for GCN4–FcεRI. The FRET signals are represented by the fluorescence lifetime of moxCerulean3 in 293T cells. Compared with donor wild-type FcεRI only, the presence of acceptor wild-type FcεRI yielded a decreased fluorescence lifetime (column 1). The decreased signal disappeared upon IgE binding (column 2). 'Donor only' refers to cells transfected with moxCerulean3-labelled FcεRI. 'Donor + acceptor' refers to cells co-expressing moxCerulean3-labelled and mGold-labelled FcεRI. The total number of cells in each group is shown. **e**, FRET signals are represented by FRET efficiency in cells expressing FcεRI variants with and without IgE. The mean of each donor-only group was used to calculate the FRET efficiency in each donor-plus-acceptor group. Data are mean ± s.e.m. and the total number of cells in each group is shown. **d**,**e**, Data were analysed from three independent experiments. *P* values were calculated using one-way ANOVA followed by Games–Howell's multiple-comparison test.

a GCN4–FcεRI dimer and an IgE (2 × 145 kDa + 195 kDa = 485 kDa). As previously suggested, owing to steric hindrance, the GCN4–FcεRI dimer can only engage one molecule of IgE.

Next, we examined the oligomeric state of FcεRI on cell membranes using fluorescence lifetime imaging and Förster resonance energy transfer (FLIM–FRET). We fused either CFP or YFP onto the C terminus of the α subunit. Both the α-CFP (donor) and α-YFP (acceptor) subunits were co-expressed with the β and γ subunits in cells. We then evaluated the fluorescence lifetime (Fig. 4d) and FRET efficiency (Fig. 4e). Compared with donor wild-type FcεRI only, the presence of acceptor wild-type FcεRI yielded a decreased fluorescence lifetime (Fig. 4d) and a substantial FRET signal (Fig. 4e), suggesting dimer-mediated FRET. Co-expression with IgE led to disappearance of these signals for wild-type FcεRI (Fig. 4d,e), suggesting dimer-to-monomer transition. By contrast, the fluorescence lifetime and the FRET signal of the constitutive GCN4–FcεRI dimer were unaffected by IgE expression (Fig. 4d,e).

In conclusion, our biochemical and cell-based assays demonstrate that upon IgE engagement, dimeric FcεRI dissociates into monomers, with each FcεRI binding to one IgE molecule.

Functional implications dimer-to-monomer transition

To investigate the functional consequence of FcεRI dimer-to-monomer transition, we generated three distinct cell lines based on the rat basophil line RBL-2H3[38]. Two cell lines exhibited stable expression of either human wild-type FcεRI or GCN4–FcεRI, with the latter designed to maintain constitutive dimer formation of FcεRI. The third cell line stably expressed the human FcεRI variant that contains the mutations K117D/Y131A (FcεRI(DA)) in the ECDα. FcεRI(DA) is known to abolish IgE binding[39].

First, we evaluated the amount of FcεRI on the plasma membrane for each cell line (Fig. 5a). Compared with the control RBL-2H3 cells, all three engineered cell lines showed abundant and comparable levels of FcεRI expression on the cell surface. Next, we assessed IgE binding to the three FcεRI variants on the plasma membrane (Fig. 5b). As anticipated, cells expressing FcεRI(DA) did not bind IgE. Notably, cells expressing wild-type FcεRI exhibited markedly stronger IgE staining compared with those expressing GCN4–FcεRI. This result is consistent with our prior biochemical analysis (Fig. 4c–e) and suggests a weaker avidity towards IgE by the dimeric GCN4–FcεRI compared with wild-type FcεRI.

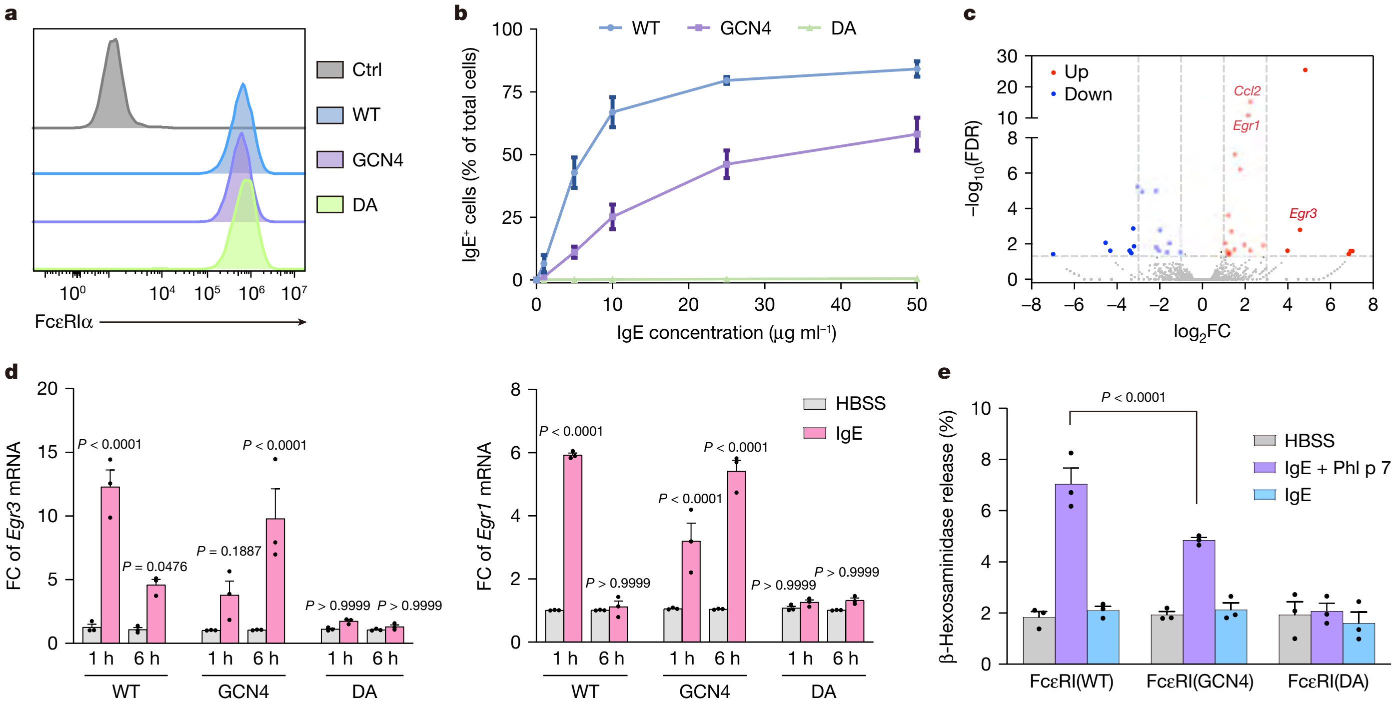

Fig. 5 | Functional consequence of FcεRI dimer-to-monomer transition. **a**, Wild-type FcεRIα and its variants are abundantly expressed in RBL-2H3 cells, as shown by flow cytometry analysis. Ctrl, no FcεRI; GCN4, expression of GCN4–FcεRIα; DA, expression of FcεRIα(K117D/Y131A). The DA mutations (K117D/Y131A) in ECDα effectively abolish IgE binding[39]. Results are representative of three independent experiments. **b**, Wild-type FcεRIα exhibits greater avidity towards IgE compared with GCN4–FcεRIα. Each FcεRI variant was exposed to increasing concentrations of IgE in the FACS assay. Data are mean ± s.d. ($n = 5$ biological replicates per group). Results are representative of two independent experiments. **c**, Volcano plot of RNA-seq results following treatment of RBL-2H3 cells with IgE, which results in alteration of gene expression. Results are representative of two independent experiments. **d**, Differential activation by IgE of *Egr3* and *Egr1* in cells expressing wild-type FcεRI versus cells expressing GCN4–FcεRI. Graphs show results of qPCR for *Egr3* (left) and *Egr1* (right). qPCR was performed 1 h and 6 h after IgE treatment. **e**, Wild-type FcεRI$^+$ cells exhibit a stronger degranulation response compared with GCN4–FcεRI$^+$ cells upon stimulation by IgE and its antigen Phl p 7. IgE and allergen treatment induced degranulation of RBL-2H3 cells. Cells were sensitized with 102.1F10 IgE[40], followed by stimulation without (blue bars) or with 0.025 μg ml^{-1} Phl p 7 (purple bars), or with HBSS (grey bars). **d**,**e**, Data are mean ± s.e.m.; each symbol corresponds to a biological replicate ($n = 3$ per group). Results are representative of three independent experiments. One-way ANOVA with Bonferroni multiple-comparison test.

The reduced avidity for IgE is presumably caused by the dimeric nature of GCN4–FcεRI.

To investigate the downstream events of IgE-mediated basophil activation, we examined the effect of IgE treatment on wild-type FcεRI$^+$ RBL-2H3 cells. Total RNAs from these cells were extracted and subjected to RNA-sequencing (RNA-seq) analysis. Compared with controls treated with Hank's Balanced Salt Solution (HBSS), 39 differentially expressed genes (DEGs) were identified in the IgE-treated wild-type FcεRI$^+$ cells on the basis of fold change (FC) >2 and false discovery rate (FDR) <0.05 (Fig. 5c). Among these genes, *Egr1*, *Egr3* and *Ccl2* were found to be related to immune response.

These three representative IgE-responsive genes were validated by quantitative PCR (qPCR) analysis at 2 time points after IgE treatment: 1 h and 6 h. In wild-type FcεRI$^+$ RBL-2H3 cells, the fold change of *Egr3* mRNA after 1 h was greater than that after 6 h, suggesting an immediate activation falling off over time (Fig. 5d, left). Of note, in GCN4–FcεRI$^+$ RBL-2H3 cells, the fold change of *Egr3* mRNA after 1 h was smaller than that after 6 h, suggesting a slow activation process. A similar pattern was also observed for *Egr1* (Fig. 5d, right). In all cases, FcεRI(DA)$^+$ cells were indifferent to IgE treatment (Fig. 5d and Extended Data Fig. 9a).

The *Ccl2* gene behaved differently. In both wild-type FcεRI$^+$ and GCN4–FcεRI$^+$ cells, the fold change of *Ccl2* mRNA after 1 h was smaller than that after 6 h (Extended Data Fig. 9a), suggesting a slower activation process compared to the *Egr1* and *Egr3* genes. We speculate that, after some time, the fold change of *Ccl2* mRNA would begin to decrease in wild-type FcεRI$^+$ cells, but not in GCN4–FcεRI$^+$ cells. As a result, the activation process of the *Ccl2* gene in GCN4–FcεRI$^+$ cells may also be slower than that in wild-type FcεRI$^+$ cells. Collectively, these qPCR results demonstrate that the transcription of *Egr3*, *Egr1* and *Ccl2* genes was differentially altered in the wild-type FcεRI$^+$ versus GCN4–FcεRI$^+$ cells. Such alteration could be accounted for by the impaired dimer-to-monomer transition of GCN4–FcεRI upon IgE engagement.

Finally, we evaluated the effect of FcεRI dimer-to-monomer transition on antigen-dependent response using a degranulation assay (Extended Data Fig. 9b). Upon stimulation by a patient-derived antibody (102.1F10 IgE) and the Timothy grass pollen allergen Phl p 7[40,41], the wild-type FcεRI$^+$ RBL-2H3 cells undertook pronounced degranulation. Notably, the wild-type FcεRI$^+$ cells showed a stronger degranulation response compared with the GCN4–FcεRI$^+$ cells upon stimulation by IgE and its antigen Phl p 7 (Fig. 5e). This result suggests that the dimer-to-monomer transition of FcεRI may also affect antigen-dependent responses.

Discussion

It is well established that IgE binding to its receptor FcεRI mediates mast cell activation even in the absence of an antigen[3,4,18], but the underlying mechanism has remained unknown. The structure of FcεRI reveals a dimeric organization, with the ITAMs located close to each other near the intracellular juxtamembrane region (Fig. 6a, left). Such close proximity potentially disfavours association with downstream kinases owing to steric hindrance. Therefore, we propose that dimeric FcεRI on cell membranes represents an inactive or resting state. Upon IgE engagement, FcεRI undergoes a dimer-to-monomer transition, enabling the

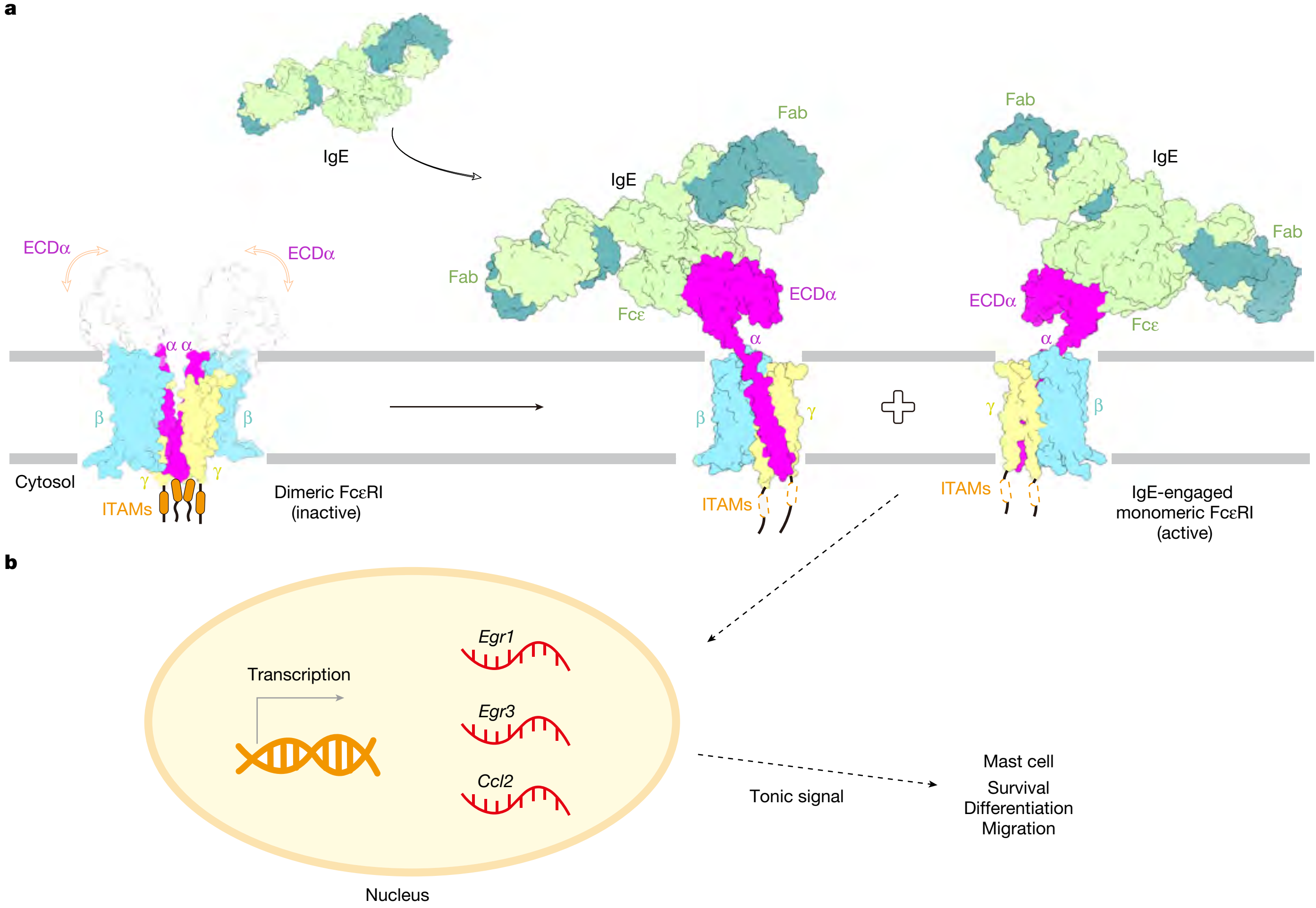

Fig. 6 | A working model of IgE-mediated responses. a, A schematic diagram showing the FcεRI dimer-to-monomer transition upon IgE engagement at the cell surface. Prior to IgE binding, FcεRI exists as a homodimer, with the ITAMs in close proximity to each other. Such a tight organization of the ITAMs may impede the action of downstream kinases. Upon IgE binding, the dimeric FcεRI is dissociated into two protomers, in which the ITAMs are more accessible to downstream kinases. Thus the dimeric FcεRI is in an inactive state, whereas the IgE-engaged FcεRI is in an active state. **b**, The FcεRI dimer-to-monomer transition induces the transcription of *Egr1*, *Egr3* and *Ccl2* in rat basophils. Accumulating evidence suggests that the expression of these genes is involved in the survival, differentiation and migration of mast cells[18,22,25,42–45].

less crowded ITAMs to engage downstream signalling kinases (Fig. 6a, right). Therefore, the IgE-engaged FcεRI is in an active state. Our model is consistent with prior findings that IgE-mediated responses rely on the ITAMs of the γ subunits[19,25].

We demonstrated that the FcεRI dimer-to-monomer transition induces the transcription of *Egr1*, *Egr3* and *Ccl2* in rat basophils (Fig. 6b). Mounting evidence suggests that the transcription factor *Egr1* is upregulated in cultures containing IgE and is involved in the production of TNF in mast cells[42]. TNF has a role in mediating IL-3-dependent differentiation of mast cells[18,42,43]. In addition, *Ccl2* is known to facilitate IgE-mediated mast cell migration[18,44]. It is noteworthy that *Egr1*, *Egr3* and *Ccl2* operate within the same signalling cascade in mast cells, regulating the phosphorylation of ERK1/2[45], which is critical for IgE-mediated mast cell survival[22,25].

Dimeric GCN4 motifs were fused to the C termini of the α chains, connected by flexible linkers, to generate GCN4–FcεRI. This design was intended to lock FcεRI in a dimeric state. AUC analysis confirmed that IgE binding did not induce a transition to a monomer (Fig. 4c). However, in the AUC conditions, the two FcεRI molecules, which were connected via their respective GCN4 leucine zippers, may not form the dimeric interface observed in our cryo-EM structure. Similarly, on the cell membrane, IgE binding may cause the dissociation of transmembrane domains of FcεRI due to clashes between the two ECDα domains, although the C termini remain linked by the GCN4 motifs. These GCN4 motifs may impede, but not completely prevent, the dimer-to-monomer transition. Consistent with this scenario, cells expressing GCN4–FcεRI$^+$ show slower activation upon IgE engagement compared with those expressing wild-type FcεRI$^+$, rather than complete inhibition (Fig. 5d and Extended Data Fig. 9a).

In our study, cholesterol-like molecules were embedded in the transmembrane domain of FcεRI, potentially stabilizing the dimeric state of apo FcεRI. In αβ and γδ T cell receptor–CD3 complexes, cholesterol-like molecules are wedged into the transmembrane domains, exerting an inhibitory effect on receptor function[46,47]. FcεRI signalling has previously been shown to be disrupted following pharmacological removal of cholesterol[48]. Our structure indicates that cholesterol molecules are crucial for the structural integrity and stability of FcεRI. Nonetheless, the multi-faceted regulatory roles of cholesterol in FcεRI function remain to be scrutinized in future studies.

The Fc receptors, expressed in various immune cells, trigger and regulate a range of cellular responses. The crosslinking of other Fc receptors, such as FcαRI and FcγRI, also elicits cell activation, endocytosis and phagocytosis[49,50]. However, the oligomeric state of these receptors remains unclear, and whether these receptors operate similarly to FcεRI remains to be investigated. Previous structural studies have focused solely on the recognition of Fc receptors by antibodies, with little information on the transmembrane domain. Our biochemical, cellular and structural studies on FcεRI reveal the molecular mechanism of IgE-mediated mast cell or basophil activation. These advances constitute an important step towards mechanistic understanding of the Fc receptor activation and may reveal additional clues for the treatment of allergies.

Online content

Any methods, additional references, Nature Portfolio reporting summaries, source data, extended data, supplementary information, acknowledgements, peer review information; details of author contributions and competing interests; and statements of data and code availability are available at https://doi.org/10.1038/s41586-024-08229-8.

1. Kay, A. B. Allergy and allergic diseases. *New Engl. J. Med.* **344**, 30–37 (2001).
2. Gould, H. J. & Sutton, B. J. IgE in allergy and asthma today. *Nat. Rev. Immunol.* **8**, 205–217 (2008).
3. Kawakami, T. & Galli, S. J. Regulation of mast-cell and basophil function and survival by IgE. *Nat. Rev. Immunol.* **2**, 773–786 (2002).
4. Galli, S. J. & Tsai, M. IgE and mast cells in allergic disease. *Nat. Med.* **18**, 693–704 (2012).
5. Galli, S. J., Gaudenzio, N. & Tsai, M. Mast cells in inflammation and disease: recent progress and ongoing concerns. *Annu. Rev. Immunol.* **38**, 49–77 (2020).
6. Kinet, J.-P. The high-affinity IgE receptor (FcεRI): from physiology to pathology. *Annu. Rev. Immunol.* **17**, 931–972 (1999).
7. Kraft, S. & Kinet, J. P. New developments in FcεRI regulation, function and inhibition. *Nat. Rev. Immunol.* **7**, 365–378 (2007).
8. Turner, H. & Kinet, J.-P. Signalling through the high-affinity IgE receptor FcεRI. *Nature* **402**, 24–30 (1999).
9. Yu, W., Freeland, D. M. H. & Nadeau, K. C. Food allergy: immune mechanisms, diagnosis and immunotherapy. *Nat. Rev. Immunol.* **16**, 751–765 (2016).
10. Kanellopoulos, J. M., Liu, T. Y., Poy, G. & Metzger, H. Composition and subunit structure of the cell receptor for immunoglobulin E. *J. Biol. Chem.* **255**, 9060–9066 (1980).
11. Perez-Montfort, R., Kinet, J. P. & Metzger, H. A previously unrecognized subunit of the receptor for immunoglobulin E. *Biochemistry* **22**, 5722–5728 (1983).
12. Weiss, A. & Littman, D. R. Signal transduction by lymphocyte antigen receptors. *Cell* **76**, 263–274 (1994).
13. Garman, S. C., Wurzburg, B. A., Tarchevskaya, S. S., Kinet, J. P. & Jardetzky, T. S. Structure of the Fc fragment of human IgE bound to its high-affinity receptor FcεRIα. *Nature* **406**, 259–266 (2000).
14. Garman, S. C., Kinet, J. P. & Jardetzky, T. S. Crystal structure of the human high-affinity IgE receptor. *Cell* **95**, 951–961 (1998).
15. Turner, H. & Kinet, J. P. Signalling through the high-affinity IgE receptor FcεRI. *Nature* **402**, B24–B30 (1999).
16. Lin, S., Cicala, C., Scharenberg, A. M. & Kinet, J. P. The FcεRIβ subunit functions as an amplifier of FcεRIγ-mediated cell activation signals. *Cell* **85**, 985–995 (1996).
17. Metzger, H. et al. The receptor with high affinity for immunoglobulin E. *Annu. Rev. Immunol.* **4**, 419–470 (1986).
18. Kashiwakura, J., Otani, I. M. & Kawakami, T. Monomeric IgE and mast cell development, survival and function. *Adv. Exp. Med. Biol.* **716**, 29–46 (2011).
19. Kitaura, J. et al. Early divergence of Fcε receptor I signals for receptor up-regulation and internalization from degranulation, cytokine production, and survival. *J. Immunol.* **173**, 4317–4323 (2004).
20. Sakurai, D. et al. FcεRIγ–ITAM is differentially required for mast cell function in vivo. *J. Immunol.* **172**, 2374–2381 (2004).
21. Asai, K. et al. Regulation of mast cell survival by IgE. *Immunity* **14**, 791–800 (2001).
22. Kalesnikoff, J. et al. Monomeric IgE stimulates signaling pathways in mast cells that lead to cytokine production and cell survival. *Immunity* **14**, 801–811 (2001).
23. Kitaura, J. et al. Evidence that IgE molecules mediate a spectrum of effects on mast cell survival and activation via aggregation of the FcεRI. *Proc. Natl Acad. Sci. USA* **100**, 12911–12916 (2003).
24. Matsuda, K. et al. Monomeric IgE enhances human mast cell chemokine production: IL-4 augments and dexamethasone suppresses the response. *J. Allergy Clin. Immunol.* **116**, 1357–1363 (2005).
25. Yamasaki, S. & Saito, T. Progress in allergy signal research on mast cells: signal regulation of multiple mast cell responses through FcεRI. *J. Pharmacol. Sci.* **106**, 336–340 (2008).
26. Bryce, P. J. et al. Immune sensitization in the skin is enhanced by antigen-independent effects of IgE. *Immunity* **20**, 381–392 (2004).
27. Gurish, M. F. et al. IgE enhances parasite clearance and regulates mast cell responses in mice infected with *Trichinella spiralis*. *J. Immunol.* **172**, 1139–1145 (2004).
28. Altrichter, S. et al. Total IgE as a marker for chronic spontaneous urticaria. *Allergy Asthma Immunol. Res.* **13**, 206–218 (2021).
29. Cugno, M. et al. Elevated IgE to tissue factor and thyroglobulin are abated by omalizumab in chronic spontaneous urticaria. *Allergy* **73**, 2408–2411 (2018).
30. McDonnell, J. M., Dhaliwal, B., Sutton, B. J. & Gould, H. J. IgE, IgE receptors and anti-IgE biologics: protein structures and mechanisms of action. *Annu. Rev. Immunol.* **41**, 255–275 (2023).
31. Yan, N., Wu, J. W., Chai, J., Li, W. & Shi, Y. Molecular mechanisms of DrICE inhibition by DIAP1 and removal of inhibition by Reaper, Hid and Grim. *Nat. Struct. Mol. Biol.* **11**, 420–428 (2004).
32. Kirshenbaum, A. S. et al. Characterization of novel stem cell factor responsive human mast cell lines LAD 1 and 2 established from a patient with mast cell sarcoma/leukemia; activation following aggregation of FcεRI or FcγRI. *Leuk. Res.* **27**, 677–682 (2003).
33. Glassman, C. R. et al. Structure of a Janus kinase cytokine receptor complex reveals the basis for dimeric activation. *Science* **376**, 163–169 (2022).
34. Mirdita, M. et al. ColabFold: making protein folding accessible to all. *Nat. Methods* **19**, 679–682 (2022).
35. Su, Q. et al. Cryo-EM structure of the human IgM B cell receptor. *Science* **377**, 875–880 (2022).
36. Dong, D. et al. Structural basis of assembly of the human T cell receptor–CD3 complex. *Nature* **573**, 546–552 (2019).
37. Hatada, M. H. et al. Molecular basis for interaction of the protein tyrosine kinase ZAP-70 with the T-cell receptor. *Nature* **377**, 32–38 (1995).
38. Barsumian, E. L., Isersky, C., Petrino, M. G. & Siraganian, R. P. IgE-induced histamine release from rat basophilic leukemia cell lines: isolation of releasing and nonreleasing clones. *Eur. J. Immunol.* **11**, 317–323 (1981).
39. Mackay, G. A. et al. Mutagenesis within human FcεRIα differentially affects human and murine IgE binding. *J. Immunol.* **168**, 1787–1795 (2002).
40. James, L. K. et al. Allergen specificity of IgG$_4$-expressing B cells in patients with grass pollen allergy undergoing immunotherapy. *J. Allergy Clin. Immunol.* **130**, 663–670.e663 (2012).
41. Mitropoulou, A. N. et al. Structure of a patient-derived antibody in complex with allergen reveals simultaneous conventional and superantigen-like recognition. *Proc. Natl Acad. Sci. USA* **115**, E8707–E8716 (2018).
42. Kashiwakura, J. et al. Pivotal advance: IgE accelerates in vitro development of mast cells and modifies their phenotype. *J. Leukoc. Biol.* **84**, 357–367 (2008).
43. Wright, H. V. et al. IL-3-mediated TNF production is necessary for mast cell development. *J. Immunol.* **176**, 2114–2121 (2006).
44. Kitaura, J. et al. IgE$^-$ and IgE$^+$ Ag-mediated mast cell migration in an autocrine/paracrine fashion. *Blood* **105**, 3222–3229 (2005).
45. Wang, H. N. et al. Inhibition of c-Fos expression attenuates IgE-mediated mast cell activation and allergic inflammation by counteracting an inhibitory AP1/Egr1/IL-4 axis. *J. Transl. Med.* **19**, 261 (2021).
46. Xin, W. et al. Structures of human gammadelta T cell receptor–CD3 complex. *Nature* **630**, 222–229 (2024).
47. Chen, Y. et al. Cholesterol inhibits TCR signaling by directly restricting TCR–CD3 core tunnel motility. *Mol. Cell* **82**, 1278–1287.e1275 (2022).
48. Sheets, E. D., Holowka, D. & Baird, B. Critical role for cholesterol in Lyn-mediated tyrosine phosphorylation of FcεRI and their association with detergent-resistant membranes. *J. Cell Biol.* **145**, 877–887 (1999).
49. Nimmerjahn, F. & Ravetch, J. V. Fcγ receptors as regulators of immune responses. *Nat. Rev. Immunol.* **8**, 34–47 (2008).
50. Daeron, M. Fc receptor biology. *Annu. Rev. Immunol.* **15**, 203–234 (1997).
51. Pettersen, E. F. et al. UCSF ChimeraX: structure visualization for researchers, educators, and developers. *Protein Sci.* **30**, 70–82 (2021).

Methods

Plasmids and constructs

The cDNAs encoding the human FcεRI α subunit, β subunit and γ subunit were codon-optimized and synthesized by Tsingke Biotechnology and individually subcloned into the optimized pCAG vector. A synthetic signal peptide (MDMRVPAQLLGLLLLWLSGARC)[52] was fused to the N terminus of the α subunit. A Flag tag (MDYKDDDDK) and a twin-Strep II tag were fused to the C and N termini of the α and β subunits, respectively (Fig. 1a). For GCN4–FcεRI, the leucine zipper motif (RMKQLE DKVEELLSKNYHLENEVARLKKLVGER) was fused to the C terminus of the Flag tag on the α subunit. Human 102.1F10 IgE and anti-gp120 IgE coding sequences were codon-optimized, with the synthetic signal peptide at its N terminus and an 8×His tags at its C terminus. The cDNAs encoding Timothy grass pollen allergen Phl p 7 is also codon-optimized, with an 8×His tag at its C terminus, and then subcloned into pET21b vector. Detailed information regarding these constructs is provided in the supplementary information.

Purification of FcεRI

As previously described[35,53], 2 mg of plasmids (0.6 mg each for the α and β subunits and 0.8 mg for the γ subunit) were pre-incubated with 4 mg of 40K polyethylenimines (PEIs) (Yeasen) in 40 ml of fresh medium (Sino Biological) for 15 min before being transfected into 1 liter of Expi-HEK293F cells (Thermo Fisher Scientific). Subsequently, the transfected cells were cultured at 37 °C under 5% CO_2 in a Multitron-Proshaker (Infors, 120 rpm) for another 2 days before collection. The collected cells were homogenized on ice using 25 mM HEPES pH 7.4, 150 mM NaCl, 10% (v/v) glycerol containing 1 mM PMSF, 2 μg ml^{-1} pepstatin, 2 μg ml^{-1} aprotinin and 2 μg ml^{-1} leupeptin. The cell membrane was solubilized overnight at 4 °C using 1% (w/v) lauryl maltose neopentyl glycol (LMNG) (Anatrace) and 0.2% (w/v) cholesteryl hemisuccinate (CHS). Insoluble material and cell debris were removed by centrifugation. The resulting supernatant was applied to anti-Flag M2 affinity resin (Millipore-Sigma), washed using the wash buffer (25 mM HEPES pH 7.4, 150 mM NaCl, 10% (v/v) glycerol, 0.01% (w/v) LMNG, and 0.002% (w/v) CHS), and eluted using the wash buffer supplemented with 400 μg ml^{-1} of the Flag peptide. The eluent from the anti-Flag resin was loaded onto the Strep-Tactin resin (IBA), washed using the wash buffer, and eluted using 25 mM HEPES pH 7.4, 150 mM NaCl, 0.01% (w/v) LMNG, 0.002% (w/v) CHS and 5 mM desthiobiotin. The resulting FcεRI was concentrated to 0.5 ml and further fractionated using SEC (Superose 6 increase 10/300, GE Healthcare) in the wash buffer containing 0.004% (w/v) LMNG and 0.0008% (w/v) CHS. Other FcεRI variants were purified similarly.

For the purification of IgE-bound FcεRI, the plasmids for secretory IgE and FcεRI were co-expressed, and a similar purification procedure was applied except that the detergent was changed from LMNG/CHS to glyco-diosgenin (GDN). The resulting IgE–FcεRI complexes were eluted and concentrated for SEC purification in the buffer containing 25 mM HEPES pH 7.4, 150 mM NaCl and 0.005% (w/v) GDN.

Preparation of secretory IgE

The plasmids encoding the ε and λ chains (1 mg each) were pre-mixed with 4 mg of PEI in 40 ml of fresh medium for 15 min. The mixture was then added to 1 l cell culture, and the transfected ExpiHEK293F cells were cultured at 37 °C under 5% CO_2 for another 5 days before collection. After centrifugation at 4,000*g* for 10 min, the supernatant was collected and further cleaned up using the 0.45-μm filter membrane. The resulting medium was concentrated to approximately 100 ml and loaded onto the Ni-NTA resin (Qiagen). The resin was thoroughly washed using the wash buffer (25 mM Tris, pH 8.0 and 150 mM NaCl) supplemented with additional 30 mM imidazole. The secretory IgE was eluted using the wash buffer supplemented with 300 mM imidazole, concentrated using a 50-kDa cut-off Centricon (Millipore), and further purified using SEC (Superdex 200 increase 10/300 GL) in phosphate-buffered saline (PBS) buffer. The resulting protein was flash-frozen in liquid nitrogen and stored at −80 °C for subsequent assays. The expression and purification of moxBFP-labelled IgE, in which moxBFP[54] is fused to the C terminus of the heavy chain of IgE, followed a similar protocol as described above.

Preparation of Phl p 7

Timothy grass pollen allergen Phl p 7 was expressed in *Escherichia coli* BL21 (DE3) cells. Recombinant protein expression was induced by adding 0.25 mM IPTG when the cell density reached the OD_{600} value of 0.8. Following overnight induction at 18 °C, the cells were collected using centrifugation and resuspended in a buffer containing 25 mM Tris-HCl (pH 8.0) and 150 mM NaCl, supplemented with 1 mM protease inhibitor PMSF. Cells were lysed using sonication, and the resulting lysate was cleared of debris using centrifugation at 13,000*g* for 1 h at 4 °C. The supernatant was subjected to the Ni-NTA resin (Qiagen). The resin was thoroughly washed using the buffer (25 mM HEPES, pH 7.4, 150 mM NaCl) supplemented with additional 30 mM imidazole. Phl p 7 was eluted using the same buffer supplemented with 300 mM imidazole, concentrated using a 10-kDa cut-off Centricon (Millipore), and fractionated using SEC (Superdex 200 Increase 10/300 column, GE Healthcare) in the PBS buffer.

Cryo-EM sample preparation and data collection

A 4-μl aliquot of the protein sample was applied to the holey carbon grids (Quantifoil, Au, 300-mesh or 200-mesh, R1.2/1.3), which had been glow-discharged at 15 mA for 30 s using the Plasma Cleaner PDC-32G-2 (HARRICK PLASMA Company). After 3–4 s of blotting, the grid was rapidly plunged into liquid ethane cooled by liquid nitrogen using a Vitrobot Mark IV (Thermo Scientific) under 100% humidity at 8 °C.

The grids were imaged on a Titan Krios electron microscopy (Thermo Scientific) operating at 300 kV and equipped with a Gatan K3 Summit detector and a GIF Quantum energy filter. Zero-loss movie stacks were automatically collected using EPU (Thermo Scientific) with a slit width of 20 eV on the energy filter and a preset defocus range from −1.0 μm to −2.0 μm in Aberration-free image shift (AFIS) mode with a nominal magnification[55] 81,000×. The image shift was employed, and coma was compensated during data collection, with the maximum image shift not exceeding 10 μm. Each micrograph stack, containing 32 frames, was exposed to a total electron dose of 50 $e^- Å^{-2}$ over 2.56 s.

Cryo-EM data processing of FcεRI and IgE–FcεRI complexes

The flowcharts for data processing of the FcεRI and IgE–FcεRI complexes are presented in Extended Data Figs. 1 and 6, respectively.

For the FcεRI dataset, four batches of movie stacks were motion-corrected using MotionCor2[56], and the dose-weighted micrographs were subjected to Patch contrast transfer function (CTF) estimation using cryoSPARC[57]. Micrographs exhibiting an estimated CTF resolution of worse than 4 Å and ice thickness greater than 1.1 were manually discarded, which resulted in 1,913 micrographs for dataset A, 8,284 micrographs for dataset B, 15,404 micrographs for dataset C, and 12,278 micrographs for dataset D. The combined dataset of 10,197 micrographs from A and B were subjected to both Template and Topaz picking, which led to 20,065,700 particles. These particles were subjected to multiple rounds of 2D classification, leading to 2,523,533 particles with high-resolution features. Multiple rounds of ab initio reconstruction ($K = 5$) were performed to discard heterogenous particles, resulting in 84,653 particles. Another round of ab initio reconstruction ($K = 3$) was performed, and particles belonging to good classes were selected. After Non-uniform refinement, an initial reconstruction of 6.1 Å was generated.

To enlarge the good particle dataset, simulated particles with different views were generated using the initial reconstruction of 6.1 Å, and used for retrieving good particles from the original dataset (A and B) through seed-facilitated 2D classification as previous reported[48]. Subsequently, 4,275,357 particles were selected and subjected to multiple rounds of hetero-refinement with 1 'good' and 6 'junk' references to further remove bad particles. All particles of the good classes were combined, resulting in 1,108,652 particles. In parallel, seed-facilitated 2D classification was performed with the whole dataset (A, B, C and D), resulting in a dataset of 21,639,261 particles. To obtain a more homogenous dimeric dataset, these particles were subjected to hetero-refinement (with 'monomer' and 'dimer' class as references) until more than 95% of the remaining particles were classified into the dimeric class, resulting in 4,883,363 particles belonging to 'dimer' class. Additionally, the previous dataset of 1,108,652 particles were subjected to ab initio reconstructions ($K = 6$), from which a better initial model was generated. After non-uniform refinement, a reconstruction of the dimeric receptor at 4.2 Å with a number of 224,107 particles was achieved.

To enlarge this good dataset, these particles were used to retrieve good particles from the whole dimer dataset (4,883,363 particles) through seed-facilitated 3D ab initio reconstruction, which result in a reconstruction of the FcεRI dimer at 4.1 Å based on 827,737 particles. Considering the potential pseudosymmetry of the FcεRI dimer, 827,737 particles were doubled to 1,655,474 particles through symmetry expansion, which were subjected to 3D classification ($K = 8$) with a mask covering half of the dimer. After local refinement with the same mask, A small portion of the particles (239,131) resulted in a reconstruction of FcεRI at an average resolution of 3.74 Å. These particles are further subjected to local refinement with a new mask covering the dimer, and finally result in a reconstruction of the dimeric receptor at 3.84 Å.

For the IgE–FcεRI complex, three batches of movie stacks were motion-corrected using MotionCor2[56], and dose-weighted micrographs were subjected to Patch CTF estimation using cryoSPARC[57]. Micrographs exhibiting an estimated CTF resolution of worse than 4 Å and ice thickness greater than 1.1 were manually discarded, resulting in 6,774 micrographs for dataset A, 4,581 micrographs for dataset B, and 13,311 micrographs for dataset C. 14,698,030 particles were extracted from dataset A through both Template and Topaz picking, and subjected to multiple rounds of 2D classification to remove junk particles, resulting in 2,204,574 particles with good features. These particles were subjected to two rounds of ab initio reconstruction ($K = 5$). The particles belonging to the good class were selected and subjected to non-uniform refinement, which resulted in an initial reconstruction at 4.8 Å based on 131,134 particles. Simulated datasets were then generated using this initial model, and seed-facilitated 2D classification was performed to retrieve more good particles form the whole dataset (A, B and C). All the good particles were combined to generate a dataset of 7,858,997 particles. To obtain more homogenous datasets, Hetero-refinement was performed (with 'monomer FcεRI', 'dimer FcεRI' and 'IgE–FcεRI' class as references) until almost 95% of the remaining particles were classified into the 'IgE–FcεRI' class, resulting in a more homogenous IgE–FcεRI dataset with 2,670,756 particles.

Multiple rounds of ab initio reconstruction ($K = 5$) were performed to obtain a better initial model. 201,584 particles were selected and after non-uniform refinement, led to a better reconstruction at 3.4 Å. To enlarge this good dataset, these 201,584 particles were used to retrieve good particles from the whole IgE–FcεRI dataset (2,670,756 particles) through seed-facilitated 3D ab initio reconstruction ($K = 4$), resulting in a reconstruction at 3.23 Å based on 920,752 particles. Subsequently, local refinement with a local mask led to a reconstruction at 3.19 Å. To improve the map density in the transmembrane region, the 920,752 particles were subjected to another rounds of seed-facilitated 3D ab initio reconstruction ($K = 4$). 149,815 particles were selected and subjected to non-uniform refinement, leading to a reconstruction with an improved transmembrane region at 3.55 Å. Local refinement using a local mask also led to a reconstruction with a better transmembrane region at 3.65 Å.

The resolution of reconstruction was determined using the Fourier shell correlation (FSC) 0.143 criterion in cryoSPARC v4[57]. The 3D FSC analysis for the final maps were conducted on the Remote 3DFSC Processing Server[58] (https://3dfsc.salk.edu/). All map figures were generated using ChimeraX[51] or Chimera[59].

Model building and refinement

For the IgE–FcεRI complex, the reported IgE–ECDα structure (Protein Data Bank (PDB) 8C1C) was used as an initial template. The IgE–ECDα model was docked into the cryo-EM map of the IgE–FcεRI complexes. The model of FcεRI was built based on the predicted model using AlphaFold2[34]. These models were manually checked in COOT[60] and refined using PHENIX[61]. All structural refinements were performed in PHENIX in real space, with secondary structure and geometry restraints[61]. To monitor overfitting, the models was refined against one of the two independent half maps from the gold-standard refinement approach and tested against the other map[62]. The structures were validated through examination of the Molprobity[63] scores and statistics of the Ramachandran plots (Extended Data Table 1).

Analytical ultracentrifugation

The AUC experiments were conducted in the AUC buffer (20 mM HEPES pH 7.4, 150 mM NaCl) using an Optima AUC-A/I analytical ultracentrifuge (Beckman Coulter). Diluted samples (380 µl) of different FcεRI variants solubilized in SEC buffer, along with reference solutions (400 µl), were loaded into a conventional double-sector quartz cell and mounted in a Beckman An-50 Ti rotor for sedimentation velocity analytical ultracentrifugation (SV-AUC). Intensity data were collected in continuous mode with absorbance at 280 mm using a rotor speed of 40,000 rpm at 20 °C. All raw data were analysed using SEDFIT with the continuous c(s) distribution model. The partial specific volumes ($\vec{v}$) of each sample was calculated from the amino acid sequences using the SEDNTERP software[64]. The density and viscosity of solvents were measured using the density meter DMA45000M (Anton Paar) and Viscometer Lovis 2000 M/ME (Anton Paar), respectively.

Cell culture

Human mast cell line LAD2 was provided by J. Wang and cultured in RPMI-1640 medium supplemented with 10% (v/v) fetal bovine serum (FBS, Gibco), 100 U ml^{-1} penicillin and 100 mg ml^{-1} streptomycin (Sino Biological). The RBL-2H3 cells (iCell) were cultured in MEM medium (iCell) supplemented with 15% (v/v) FBS (Gibco) and 100 U ml^{-1} penicillin/streptomycin. In addition, the Lenti-X 293T cell line was provided by Q. Huang and cultured in DMEM (Gibco) supplemented with 10% FBS (Gibco) and penicillin/streptomycin (100 U ml^{-1}) (Sino Biological). The subculture of RBL-2H3 and Lenti-X 293T cells was performed using 0.5% trypsin (Gibco) and cells were maintained at 37 °C in a 5% CO_2 incubator.

Native PAGE

To assess the oligomeric state of FcεRI profiling, LAD2 cell lysates and different SEC fractions obtained from other purified FcεRI variants were subjected to blue native gel electrophoresis. LAD2 cells corresponding to 1 mg protein amount were pelleted and solubilized in 0.8 ml lysis buffer (20 mM HEPES pH 7.4, 150 mM NaCl) containing 1% (w/v) LMNG and 0.2% CHS for 30 min on ice. The supernatant or purified FcεRI variants were mixed with 5× loading dye (100 mM Tris 6.8, 20% glycerol, 0.1% BPB and 0.2% (w/v) Coomassie G-250) and applied to a loading zone of 5 cm width. Electrophoresis was performed for 4 h at 150 mV in the running buffer (50 mM Tris, 50 mM MOPS, 1 mM EDTA, pH 7.6). After electrophoresis, the proteins on the native gel were transferred onto a PVDF membrane using eBlot L1 Fast Wet Transfer System (Genscript). FcεRI was analysed using rabbit polyclonal antibody against FcεRIα (DF6593, Affinity) and secondary goat anti-rabbit antibody (CW0103S).

Quantification and identification of cholesterol by LC–MS/MS

To examine the identity of the lipids in the sample, a total of 200 µl protein solution was reduced using 5 mM dithiothreitol (37 °C, 30 min) and alkylated using 20 mM idoacetamide (25 °C, 30 min). Following overnight digestion at 37 °C using trypsin at an enzyme-to-protein ratio of 1:50 (w/w), total lipids were extracted using methyl *tert*-butyl ether, followed by vertexing and sonication. The supernatants were lyophilized and dissolved in 200 µl methanol for subsequent liquid chromatography–mass spectrometry (LC–MS/MS) analysis.

For cholesterol detection, a SCIEX 6500+ triple-quadrupole mass spectrometer equipped with an atmospheric pressure chemical ionization (APCI) source was used in the positive mode. Cholesterol was monitored using multiple reaction monitoring, with ion transitions at m/z 369.3 ($[M+H-H_2O]^+$) > 147.3 and 369.3 > 161.2. Separation was achieved on an Acquity UPLC BEH C18 column (50 mm × 2.1 mm, 1.7 µm) at 40 °C. The mobile phase, consisting of 0.1% formic acid in water (A) and 0.1% formic acid in methanol (B), was applied at a flow rate of 0.6 ml min^{-1}. The gradient from 90% to 100% B lasted over 6 min, was held at 100% B for 2 min, returned to 90% B in 0.1 min, and was held at 90% for an additional 1.9 min. Cholesterol content was quantified using the peak area of a standard. MS/MS spectra were further obtained using an Agilent 6545 quadrupole time-of-flight mass spectrometer coupled to an Agilent 1290 ultra-performance liquid chromatography system.

FLIM–FRET measurement and analysis

For the FLIM–FRET analysis, the full-length α subunit of FcεRI or its variants were fused to CFP (moxCerulean3[54]) or YFP (mGold[65]), which served as the FRET donor or acceptor, respectively. The α subunit or its variants, β subunit, and γ subunit were subcloned into an optimized mammalian expression vector pCAG, individually separated by P2A ribosome-skipping sites (ATNFSLLKQAGDVEENPGP). The FLIM–FRET experiments were conducted using transfected HEK-293T cell. Cells were plated onto 4-chamber glass bottom dish (D35C4-20-1.5-N, Cellvis) and cultured in DMEM (Gibco) supplemented with 10% FBS (Gibco) and 1% penicillin/streptomycin (Sino Biological). Transfections were performed using Lipofectamine 3000 (Thermo Fisher Scientific) according to manufacturer's instructions. The transfected 293T cells expressing either donor only (α-moxCerulean3) or donor + receptor (α-moxCerulean3/α-mGold) were cultured for another 12 h to reach higher confluency before FLIM–FRET analysis.

Fluorescence lifetime measurements of the donor fluorophore, both in the donor only group and donor + receptor group, were conducted using a Leica STELLARIS8 microscope equipped with a confocal scan head featuring field-programmable gate array (FPGA) electronics, pulsed laser excitation at 448 nm, and fast spectral single-photon counting detectors (HyD family). Lifetime images were acquired at a rate of 400 Hz utilizing *xyz* acquisition mode, with a high spatial resolution of 512 × 512 pixels. To ensure reliable lifetime data, photons from the entire image were recorded, with a minimum of 1,000 photons per pixel captured for both donor and acceptor acquisitions. The average photon arrival per pixel was then utilized to generate FLIM images. The images were processed using the LAS X software (Leica Microsystems). The average lifetime within regions of interest (cell membrane) was determined for the cells expressing moxCerulean3 only in the donor only group, or cells expressing both moxCerulean3 and mGold in the donor + receptor group. The time-correlated single-photon counting decay curves were fitted using the mono-exponential donor fit model, enabling the calculation of the average lifetime based on multiple cells. The amplitude of each lifetime component was used to indicate its proportion, and the intensity-weighted mean τ was calculated as the average fluorescence lifetime. The FRET efficiency E was calculated according to the following equation, of which τ_{DA} and τ_D represent the quenched donor lifetime and unquenched donor lifetime, respectively.

$$E = 1 - \frac{\tau_{DA}}{\tau_D}$$

Generation of RBL-2H3 stable cell lines

The RBL-2H3 stable cell lines expressing different FcεRI variants were generated through recombinant lentivirus infection. The α chain of different FcεRI variants, along with the β and γ subunits, were separated by a P2A ribosome-skipping site (ATNFSLLKQAGDVEENPGP) and cloned into the lentiCRISPR v2 vector[66] with a spleen focus-forming virus (SFFV) promoter[67] and a mCherry[68] tag at its C terminus. Lentiviral transfer plasmids encoding different FcεRI variants, along with the packaging vectors psPAX2 and pMD2.G, were co-transfected into Lenti-X 293T cells. Transfection were performed using 40K PEIs (Yeasen) according to manufacturer's instructions. The virus was collected 48 and 72 h after transfection and further syringe-filtered (0.45 µm) (Beyotime). To increase the virus titre, 80 µg ml^{-1} protamine sulfate (Macklin) and 80 µg ml^{-1} chondroitin sulfate C (Macklin) were added to concentrate the lentivirus as previously reported[69]. The concentrated virus with 5 µg ml^{-1} polybrene (Sigma) was used to transduce RBL-2H3 cells. The transduced cells with similar red fluorescence intensities were sorted using flow cytometry to ensure similar FcεRI expression levels. Furthermore, the FITC-labelled anti-human FcεRIα antibody (Biolegend) was used to identify the surface expression level of FcεRI on the plasma membrane of RBL-2H3 cells.

Flow cytometry

For the analysis of surface expression of FcεRI in different RBL-2H3 stable cell lines, the RBL-2H3 cells expressing different FcεRI variants were incubated with FITC-labelled FcεRIα antibody for 30 min in the dark at 4 °C, followed by washing twice using the FACS buffer (PBS supplemented with 2% (v/v) FBS) before flow cytometry analysis. For the binding analysis of IgE molecules, RBL-2H3 cells expressing different FcεRI variants were suspended in 200 µl FACS buffer, incubated with IgE-moxBFP at final concentration of 0, 5, 10, 25 and 50 µg ml^{-1} at 25 °C for 30 min. Data acquisition was conducted using the Cyto-FLEX LX-5L2 (Beckman), and the data were analysed using the FlowJo software (Tree Star).

RNA-seq

RBL-2H3 cells expressing different FcεRI variants were cultured in 6-well plates and incubated with 25 µg ml^{-1} IgE in HBSS buffer at 37 °C. RBL-2H3 cells cultured in HBSS buffer were used as controls. After 1 h treatment, total RNA was isolated from the control and FcεRI-expressing RBL-2H3 cells using the FreeZol Reagent Kit (Vazyme). The RNA quality and integrity were assessed using NanoDrop One/OneC, Life Invitrogen Qubit 3.0 fluorometer and Agilent 4200 TapeStation. The RNA samples with RNA Integrity Number (RIN) above 6.5 and the 28S/18S ratio above 1.0 were selected for library preparation. In brief, mRNA was enriched using poly(T) oligo-attached magnetic beads and reverse transcribed to double-stranded cDNA, which was then subjected to adapter ligation for library construction. Sequencing was performed on the completed library and conducted on Novaseq6000 system (Illumina) for paired-end 150 bp reads. The quality control checks were performed on the raw sequencing data to remove adapters and low-quality reads using software fastp[70,71]. Then, clean reads were then aligned to the rat reference genome (Rnor_6.0) using HISAT2 (Hierarchical Indexing for Spliced Alignment of Transcripts) software[72]. Reads Count of genes were calculated using HTSeq[73]. DEG analysis was conducted using edgeR[74] to identify DEGs between the treatment and control. The significance cut-off was set at an FC value >2.0 and FDR < 0.05.

Quantitative PCR

qPCR was conducted to assess the reliability of the RNA-seq. RBL-2H3 cells expressing different FcεRI variants were seeded in 6-well plates and incubated with 25 µg ml^{-1} IgE in HBSS buffer at 37 °C for 1 h or 6 h. RBL-2H3 cells cultured in HBSS buffer served as the control. The total RNA of each sample was extracted using the FreeZol Reagent Kit

(Vazyme) and reverse transcribed to cDNA using Hifair III 1st Strand cDNA Synthesis SuperMix kit (YEASEN) following the manufacturer's instructions. qPCR was performed using a SYBR Green Master Mix kit (YEASEN) on CFX96 real-time PCR system (Bio-Rad). The expression of the housekeeping gene *ACTG1* was used as a reference for normalization. The qPCR results were analysed using the comparative threshold cycle ($\Delta\Delta C_t$) method[75] and the primer sequences are shown in Supplementary Table 1.

Cell sensitization and stimulation for degranulation assay

For the degranulation assay, RBL-2H3 cells expressing different FcεRI variants were plated onto 12-well plates at a density of 4×10^5 cells per ml per well and cultured overnight at 37 °C with 5% CO_2. Compound C48/80 (10 μg ml^{-1}) served as the positive control for degranulation. After washing with HBSS buffer (Invitrogen), the cells were sensitized by incubation with 200 ng ml^{-1} of IgE diluted in HBSS containing 1% (w/v) BSA for 5 h at 37 °C with 5% CO_2. Following three washes using the HBSS buffer, the IgE-bound FcεRI was crosslinked to allergen of different concentrations in HBSS containing 1% BSA (w/v). The β-hexosaminidase activity was measured as an indicator of degranulation.

β-Hexosaminidase activity determination

β-hexosaminidase released from RBL-2H3 cells were determined following established protocols[76]. In brief, 25 μl cell supernatants (containing secreted β-hexosaminidase) were mixed with 15 μl substrate (4 mM 4-nitrophenyl *N*-acetyl-β-D-glucosaminidase in 0.1 M citrate buffer at pH 4.5) in a 96-well plate and then incubated at 37 °C for 1 h. The supernatant of the cell lysate with 0.5% Triton X-100 (v/v) (Sigma-Aldrich) was also collected and measured to determine the cellular β-hexosaminidase activity. The reaction was terminated by adding 200 μl stop solution (0.2 M glycine, pH 10.7), and the absorbance was measured at 405 nm using a microplate reader (Varioskan LUX, Thermo). The percentage of β-hexosaminidase release was expressed as the ratio of the released β-hexosaminidase activity over the total β-hexosaminidase activity using the following equation: β-hexosaminidase release (%) = $[(OD_{secreted})/(OD_{secreted} + OD_{cellular})] \times 100$, of which OD is the optical density (absorbance), 'secreted' and 'cellular' represent the secreted and cellular β-hexosaminidase activities, respectively.

Reporting summary

Further information on research design is available in the Nature Portfolio Reporting Summary linked to this article.

Data availability

The atomic coordinates for the FcεRI dimer and the IgE–FcεRI complex have been deposited in the Protein Data Bank with the accession codes 8YVU and 8YWA, respectively. The corresponding EM maps have been deposited in the Electron Microscopy Data Bank (EMDB) with the accession codes EMD-39614 and EMD-39627. The other structural coordinates used in this study are available from PDB 8C1C and 1F6A. The RNA-seq data generated in this project are available in the Gene Expression Omnibus (GEO) repository under accession GSE278387. All materials are available from the corresponding authors upon reasonable request. Source data are provided with this paper.

52. Haryadi, R. et al. Optimization of heavy chain and light chain signal peptides for high level expression of therapeutic antibodies in CHO cells. *PLoS ONE* **10**, e0116878 (2015).
53. Su, Q. et al. Structural basis for Ca^{2+} activation of the heteromeric PKD1L3/PKD2L1 channel. *Nat. Commun.* **12**, 4871 (2021).
54. Costantini, L. M. et al. A palette of fluorescent proteins optimized for diverse cellular environments. *Nat. Commun.* **6**, 7670 (2015).
55. Lei, J. & Frank, J. Automated acquisition of cryo-electron micrographs for single particle reconstruction on an FEI Tecnai electron microscope. *J. Struct. Biol.* **150**, 69–80 (2005).
56. Zheng, S. Q. et al. MotionCor2: anisotropic correction of beam-induced motion for improved cryo-electron microscopy. *Nat. Methods* **14**, 331–332 (2017).
57. Punjani, A., Rubinstein, J. L., Fleet, D. J. & Brubaker, M. A. cryoSPARC: algorithms for rapid unsupervised cryo-EM structure determination. *Nat. Methods* **14**, 290–296 (2017).
58. Tan, Y. Z. et al. Addressing preferred specimen orientation in single-particle cryo-EM through tilting. *Nat. Methods* **14**, 793–796 (2017).
59. Pettersen, E. F. et al. UCSF Chimera—a visualization system for exploratory research and analysis. *J. Comput. Chem.* **25**, 1605–1612 (2004).
60. Emsley, P., Lohkamp, B., Scott, W. G. & Cowtan, K. Features and development of Coot. *Acta Crystallogr. D* **66**, 486–501 (2010).
61. Adams, P. D. et al. PHENIX: a comprehensive Python-based system for macromolecular structure solution. *Acta Crystallogr. D* **66**, 213–221 (2010).
62. Falkner, B. & Schroder, G. F. Cross-validation in cryo-EM-based structural modeling. *Proc. Natl Acad. Sci. USA* **110**, 8930–8935 (2013).
63. Davis, I. W. et al. MolProbity: all-atom contacts and structure validation for proteins and nucleic acids. *Nucleic Acids Res.* **35**, W375–W383 (2007).
64. Philo, J. S. SEDNTERP: a calculation and database utility to aid interpretation of analytical ultracentrifugation and light scattering data. *Eur. Biophys. J.* **52**, 233–266 (2023).
65. Lee, J. et al. Versatile phenotype-activated cell sorting. *Sci. Adv.* **6**, eabb7438 (2020).
66. Sanjana, N. E., Shalem, O. & Zhang, F. Improved vectors and genome-wide libraries for CRISPR screening. *Nat. Methods* **11**, 783–784 (2014).
67. Rintz, E. et al. Promoter considerations in the design of lentiviral vectors for use in treating lysosomal storage diseases. *Mol. Ther. Methods Clin. Dev.* **24**, 71–87 (2022).
68. Shaner, N. C. et al. Improved monomeric red, orange and yellow fluorescent proteins derived from *Discosoma* sp. red fluorescent protein. *Nat. Biotechnol.* **22**, 1567–1572 (2004).
69. Lee, J. Y. & Lee, H. H. A new chemical complex can rapidly concentrate lentivirus and significantly enhance gene transduction. *Cytotechnology* **70**, 193–201 (2018).
70. Chen, S., Zhou, Y., Chen, Y. & Gu, J. fastp: an ultra-fast all-in-one FASTQ preprocessor. *Bioinformatics* **34**, i884–i890 (2018).
71. Chen, S. Ultrafast one-pass FASTQ data preprocessing, quality control, and deduplication using fastp. *iMeta* **2**, e107 (2023).
72. Kim, D., Langmead, B. & Salzberg, S. L. HISAT: a fast spliced aligner with low memory requirements. *Nat. Methods* **12**, 357–360 (2015).
73. Anders, S., Pyl, P. T. & Huber, W. HTSeq—a Python framework to work with high-throughput sequencing data. *Bioinformatics* **31**, 166–169 (2015).
74. Robinson, M. D., McCarthy, D. J. & Smyth, G. K. edgeR: a Bioconductor package for differential expression analysis of digital gene expression data. *Bioinformatics* **26**, 139–140 (2010).
75. Schmittgen, T. D. & Livak, K. J. Analyzing real-time PCR data by the comparative C_T method. *Nat. Protoc.* **3**, 1101–1108 (2008).
76. Huang, L. et al. A rapid and sensitive assay based on particle analysis for cell degranulation detection in basophils and mast cells. *Pharmacol. Res.* **111**, 374–383 (2016).

Acknowledgements This work was supported by the Pioneer and Leading Goose R&D Program of Zhejiang (2024SSYS0029), and Start-up funds from Westlake University (to Y.S.) and Shenzhen Medical Academy of Research and Translation (to Q.S.). The work was supported by the Biomedical Data Center of Shenzhen Medical Academy of Research and Translation. The authors thank G. Huang for advice on cryo-EM data processing; X. Wang, L. Huang, Z. Jiang, Y. Gu and Y. Zhang of the Westlake University Cryo-EM facility for technical assistance; Z. Liu and L. Zheng of the Westlake University High-Performance Computing Center, P. Zhang, J. Liu and J. Pan of the Westlake University Mass Spectrometry & Metabolomics Core facility, G. Fang and M. Liao of the Westlake University Microscopy facility, and Y. Tang and B. Shen of the Westlake University Flow Cytometry facility for support; Q. Chang and W. Chu of Tsinghua University for advice on AUC data analysis; and Q. Huang and J. Wang for the generous gift of Lenti-X 293T and LAD2 cell lines, respectively.

Author contributions Q.S. conceived the project. Q.S. and M.C. designed the experiments. M.C. conducted cloning, protein purification, cryo-EM analysis and all biochemical and cell-based assays. All authors contributed to data analysis. Y.S. and Q.S. wrote the manuscript. Y.S. supervised the project.

Competing interests The authors declare no competing interests.

Additional information

Supplementary information The online version contains supplementary material available at https://doi.org/10.1038/s41586-024-08229-8.

Correspondence and requests for materials should be addressed to Qiang Su or Yigong Shi.

Peer review information *Nature* thanks Sonya Kumar Bharathkar and the other, anonymous, reviewer(s) for their contribution to the peer review of this work.

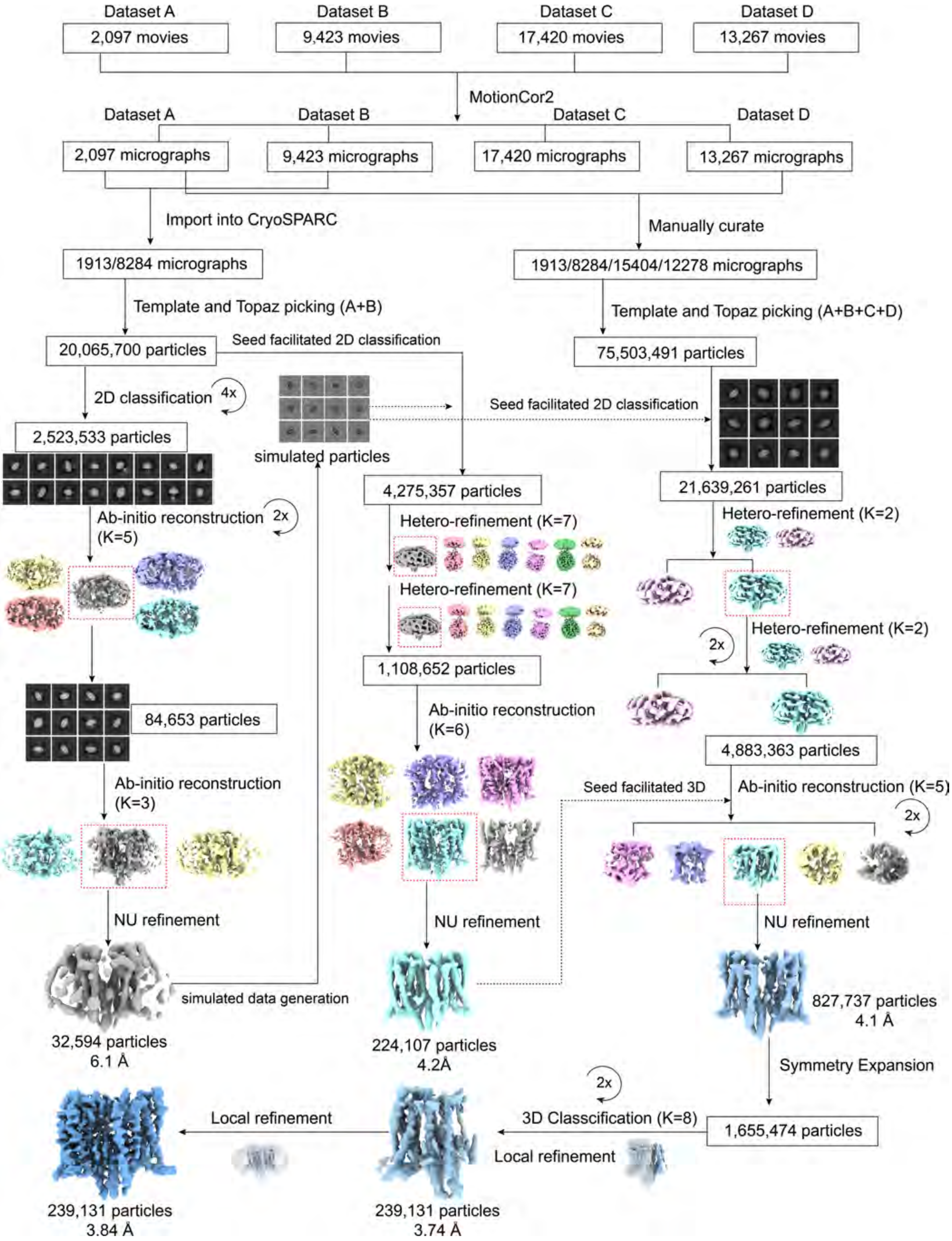

Extended Data Fig. 1 | The workflow of data processing for human FcεRI using CryoSPARC. Details are described in Methods. NU: non-uniform.

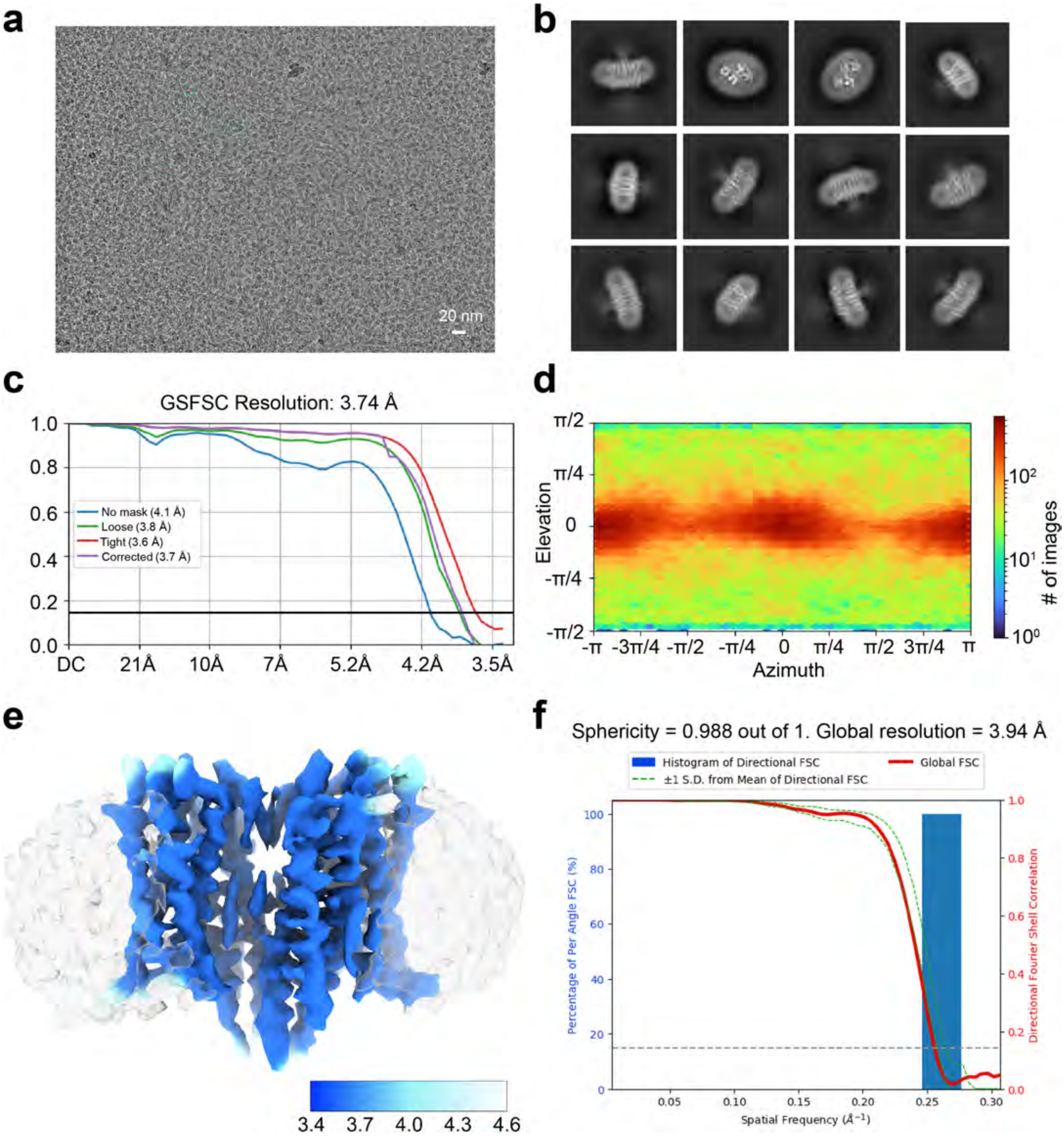

Extended Data Fig. 2 | Cryo-EM analysis of human FcεRI. a, A representative cryo-EM micrograph of human FcεRI. Results are representative of three independent experiments. **b**, Representative 2D class averages of human FcεRI. **c**, The FSC curves calculated between the independently refined half maps for human FcεRI. **d**, Angular distribution of the human FcεRI particles in the final round of 3D refinement using CryoSPARC. **e**, Color-coded local resolution estimation for the EM reconstruction of human FcεRI. The densities are contoured at 7σ. **f**, The 3DFSC sphericity plot. This plot was generated using 3DFSC[58].

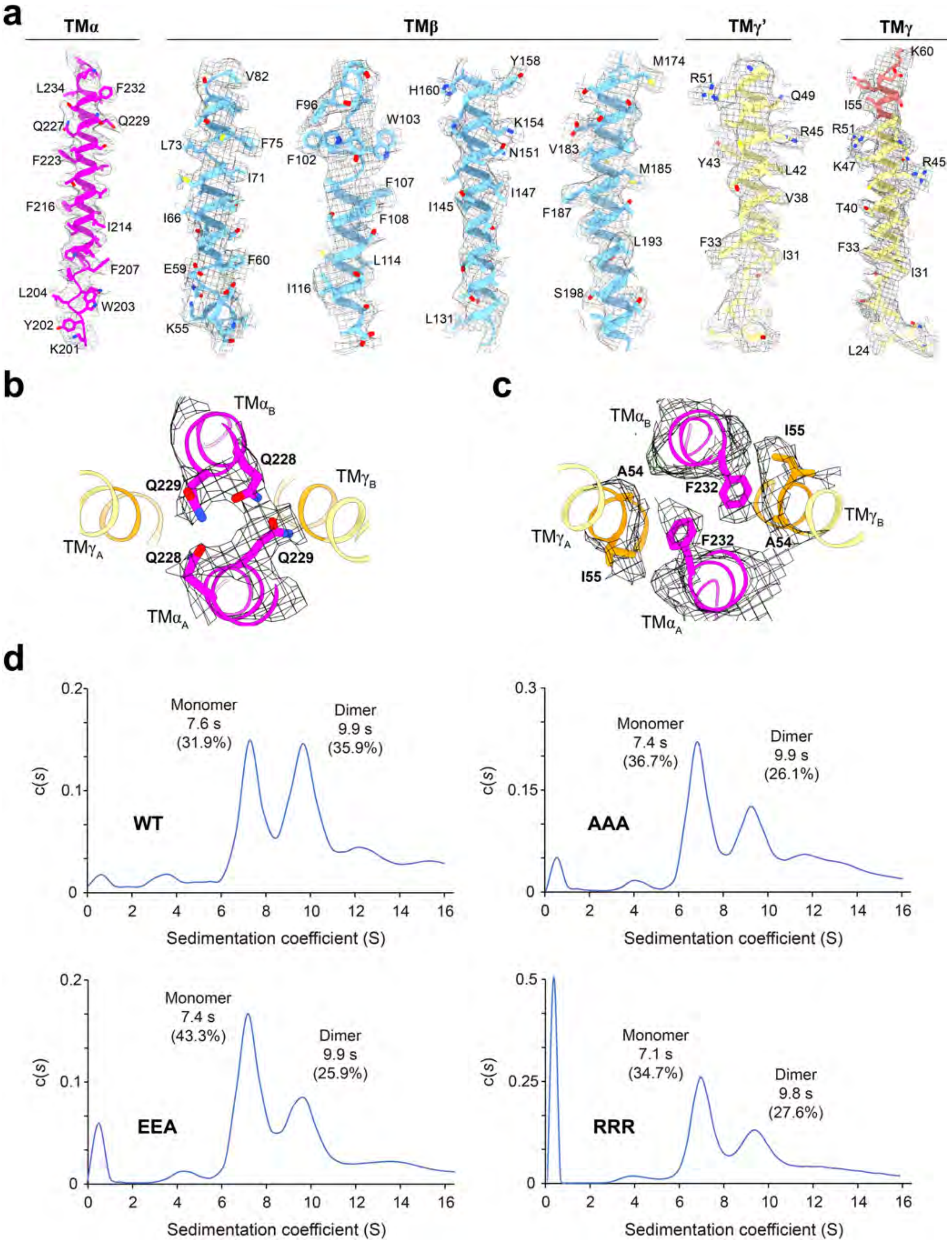

Extended Data Fig. 3 | See next page for caption.

Extended Data Fig. 3 | Representative EM maps and AUC analysis of human FcεRI. a, Representative EM maps for selected TM helices in the α, β, γ and γ′ subunits of human FcεRI. The maps, shown as grey mesh, are contoured at 5–6σ. **b-c**, Representative EM maps for the dimeric interface of FcεRI. The maps, shown as grey mesh, are contoured at 4σ. The ITAM sequences in the γ subunits are colored orange. **d**, Destabilizing mutations at the dimer interface result in increased ratios of monomer-over-dimer. Shown here are results of analytical ultracentrifugation analysis on different variants of FcεRI. The mutations are introduced in α subunits. AAA: Q228A/Q229A/F232A. EEA: Q228E/Q229E/F232A. RRR: Q228R/Q229R/F232R.

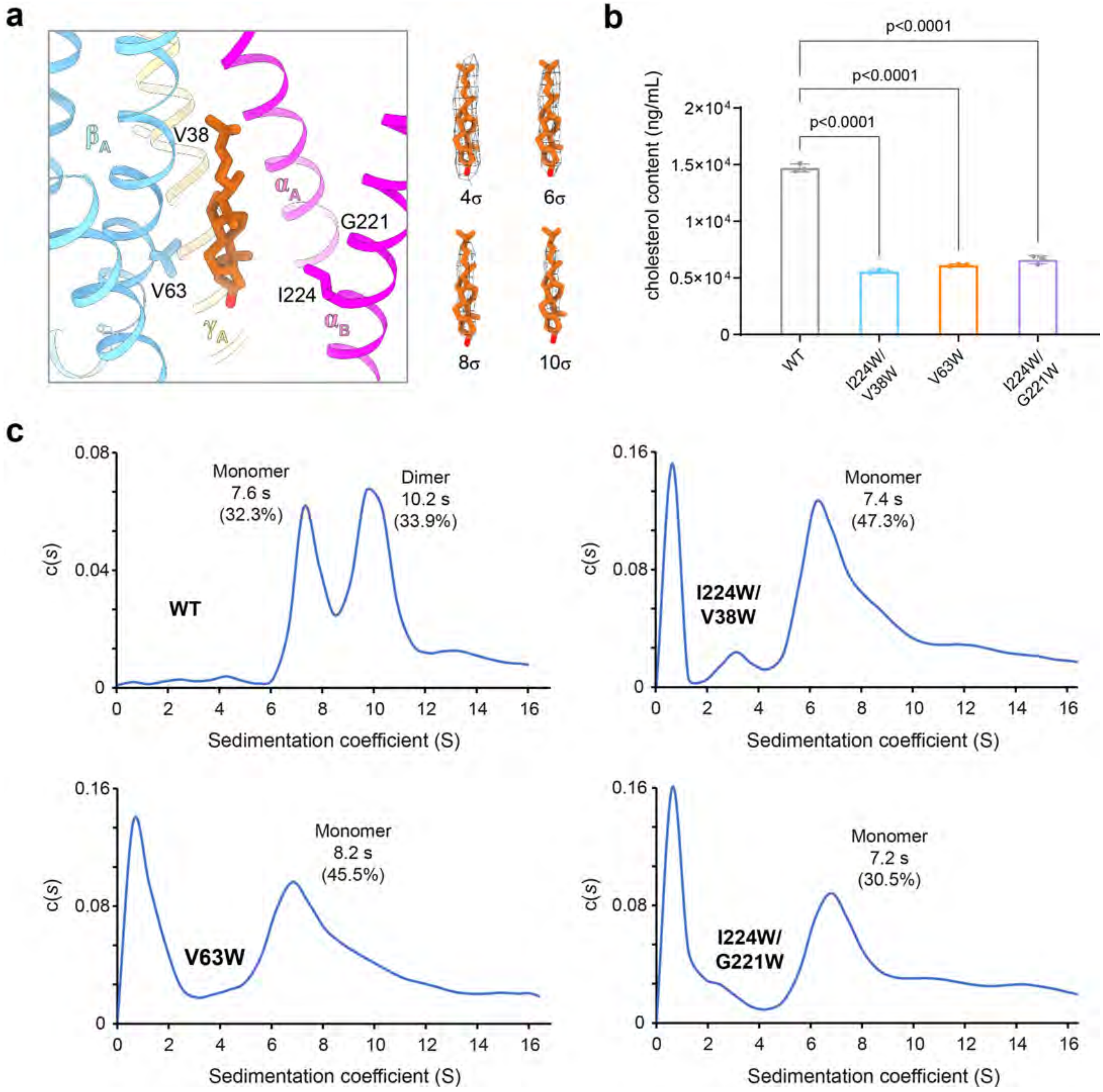

Extended Data Fig. 4 | Potential cholesterol binding site and effects of cholesterol on FcεRI dimerization. **a**, The cholesterol-like molecule is embedded in the TM domain of FcεRI. The EM density of the cholesterol-like molecule is contoured at 4σ, 6σ, 8σ, and 10σ. **b**, Quantitative analysis of cholesterol content in purified WT or mutant FcεRI complex using liquid chromatography coupled with tandem MS (LC–MS/MS; n = 3 per group). Data are mean ± SEM. *P* values were calculated using one-way ANOVA with Dunnett's multiple-comparison test. **c**, Mutations that disrupt cholesterol binding result in monomerization of FcεRI. Shown here are results of analytical ultracentrifugation analysis on three different variants of FcεRI. The mutations are introduced in the α, β, or γ subunit. The three variants are: I224W in the α chain and V38W in the γ chain (upper right), V63W in the β chain (lower left), and G221W and I224W in the α chain (lower right). WT: wild-type.

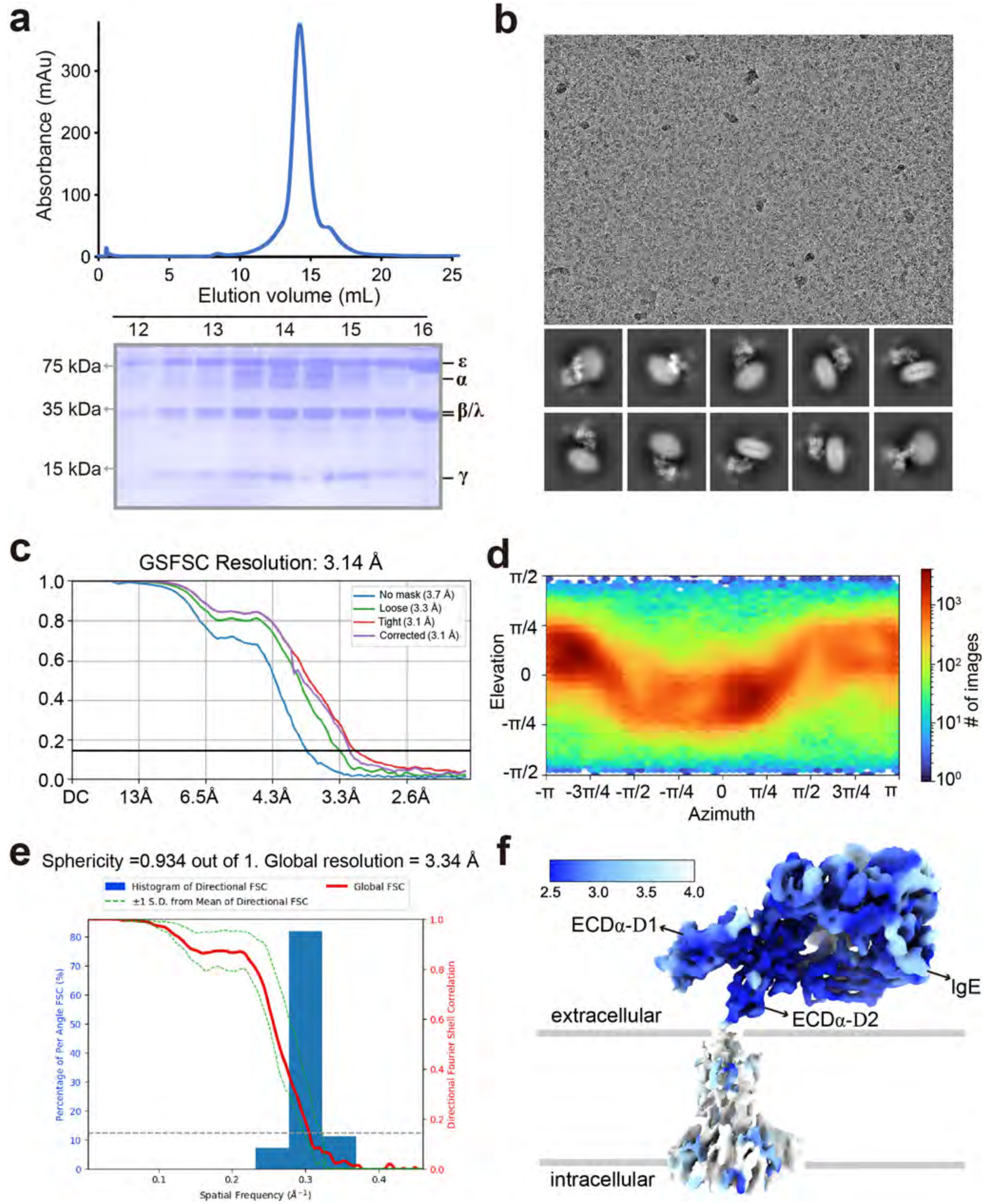

Extended Data Fig. 5 | Biochemical and cryo-EM analysis of the IgE/FcεRI complex. a, Purification of the IgE/FcεRI complex. Shown here is the SEC chromatogram for the IgE/FcεRI complex (upper panel). The peak fractions were visualized on an SDS-PAGE gel through Coomassie staining (lower panel). Results are representative of three independent experiments. **b**, A representative cryo-EM micrograph (upper panel) and 2D class averages (lower panel) of the IgE/FcεRI complex. Results are representative of three independent experiments. Scale bar: 50 nm. **c**, The FSC curves calculated between the independently refined half maps for the IgE/FcεRI complex. **d**, Angular distribution of the IgE/FcεRI particles in the final round of 3D refinement using CryoSPARC. **e**, The 3DFSC sphericity plot, generated using 3DFSC[58]. **f**, Color-coded local resolution of the EM reconstruction for the IgE/FcεRI complex. The EM map is contoured at 6σ.

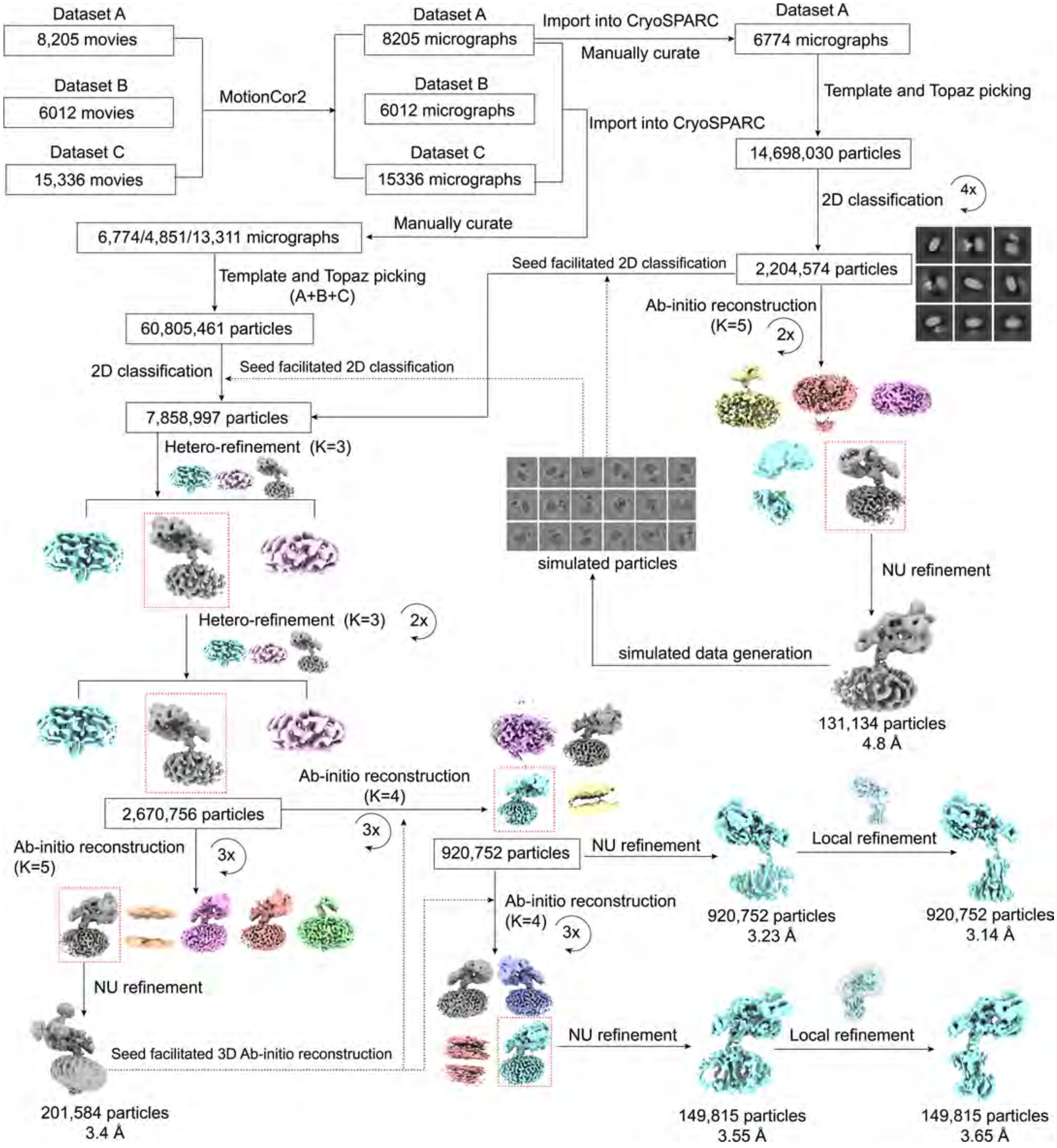

Extended Data Fig. 6 | The workflow of data processing for the IgE/FcεRI complex using CryoSPARC. Details are described in the Methods. NU: non-uniform.

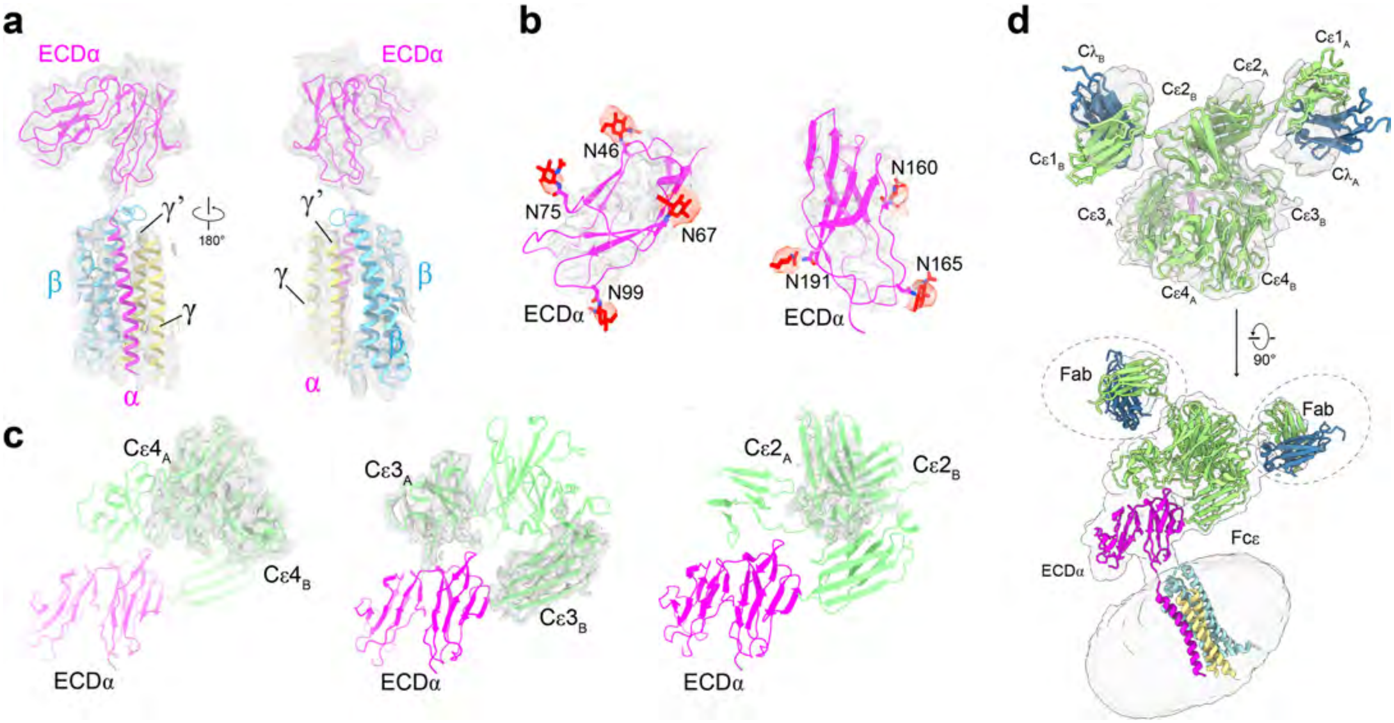

Extended Data Fig. 7 | Representative EM maps of the IgE/FcεRI complex. **a**, Two views of the EM map for FcεRI. The map, shown in transparent gray, is contoured at 10σ (left panel) or 5σ (right panel). **b**, The local EM maps for seven glycan moieties in ECDα (red). **c**, The segmented EM maps for IgE, which binds to ECDα. The maps, shown in transparent gray, are contoured at 10σ. **d**, The EM maps for IgE/FcεRI. The entire Fc domain and the Cε1/Cλ regions of both Fab domains are resolved. The maps, shown in transparent gray, are contoured at 4σ. Two perpendicular views are shown.

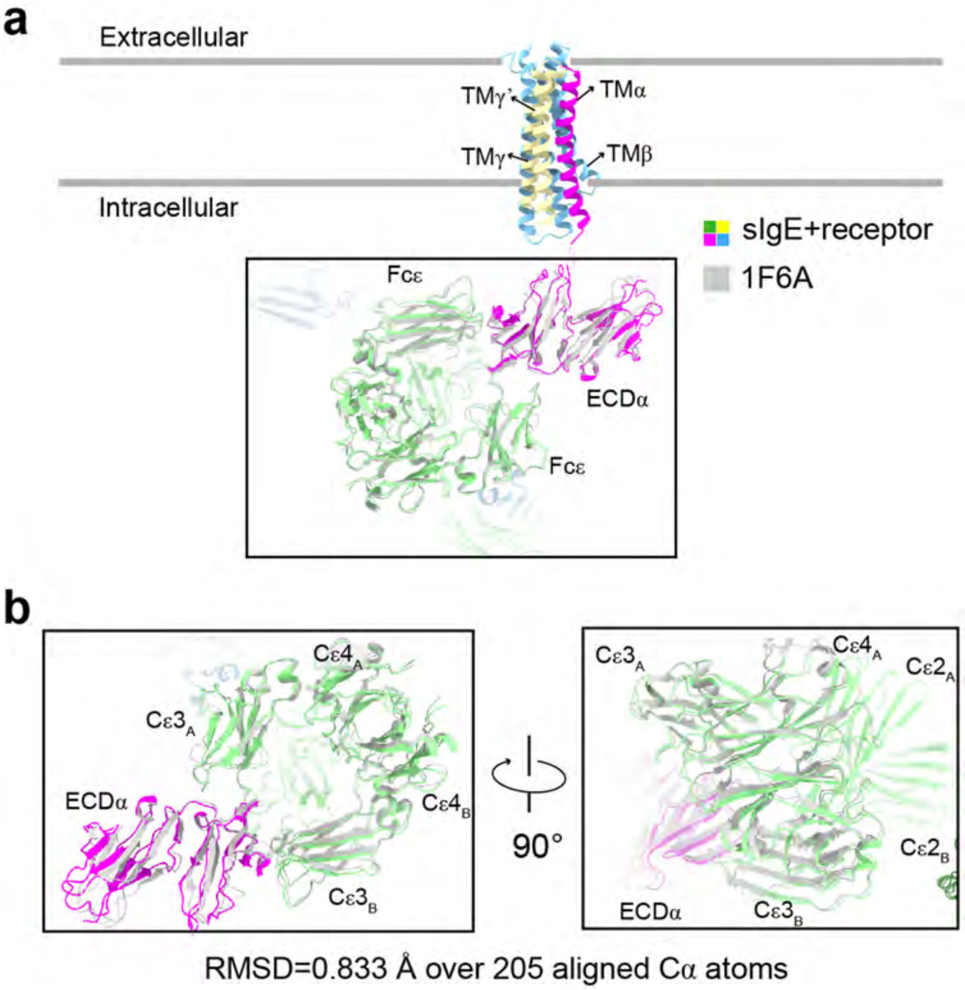

Extended Data Fig. 8 | Structure comparison between IgE-Fc/ECDα and IgE/FcεRI complex. a, The structure of IgE-Fc/ECDα[13] (PDB code: 1F6A, grey) is aligned to that of the IgE/FcεRI complex (color-coded). **b**, Two perpendicular views are shown for the extracellular portion of the IgE/FcεRI complex and its comparison with the IgE-Fc/ECDα complex.

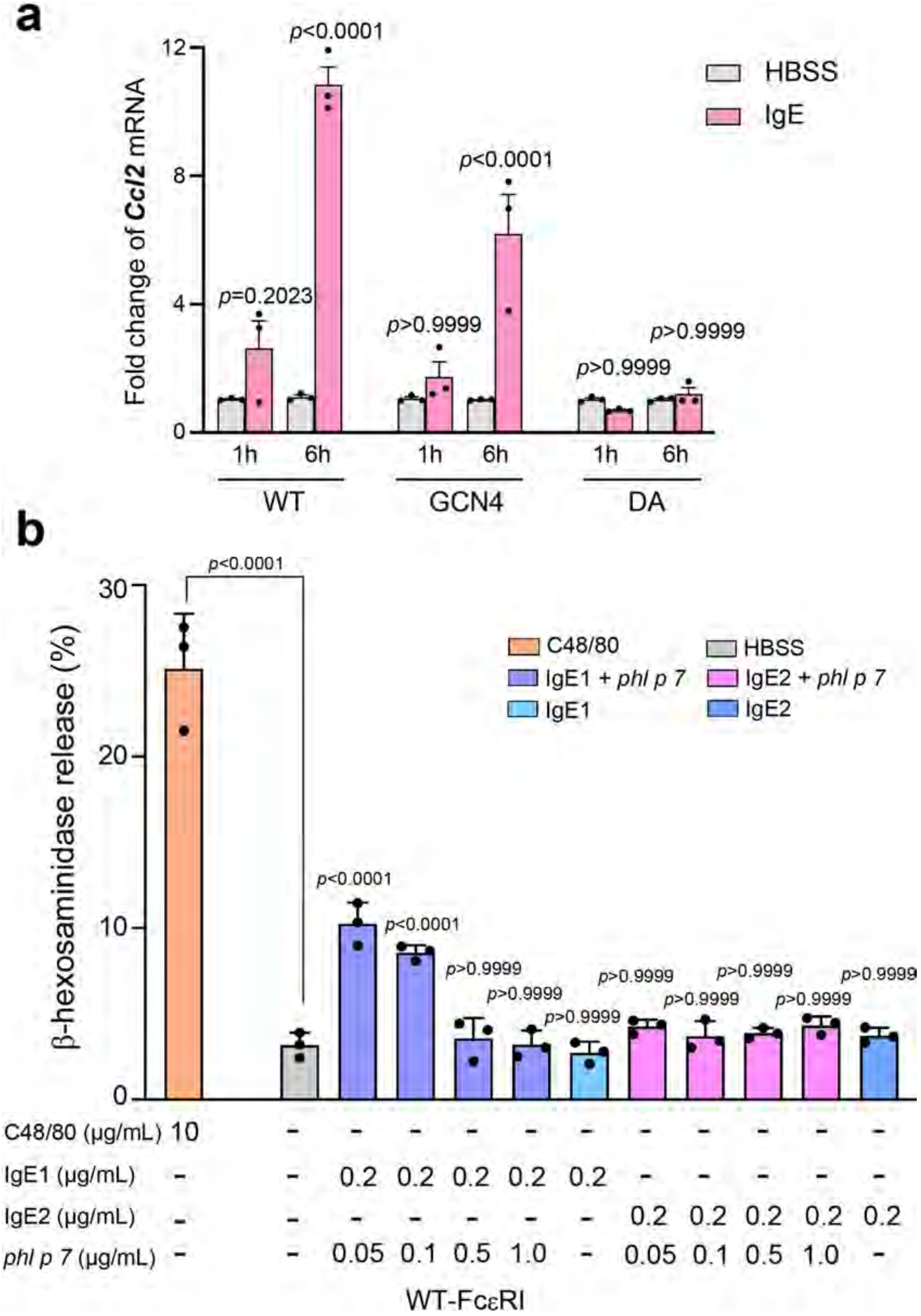

Extended Data Fig. 9 | Functional analysis of different FcεRI variants. **a**, Quantitative PCR (qPCR) analysis of the IgE-responsive gene *Ccl2* in RBL-2H3 cells with different FcεRI variants. qPCR results of the IgE-responsive gene *Ccl2* in WT-FcεRI$^+$, GCN4-FcεRI$^+$, and DA-FcεRI$^+$ cells are shown for the 1-hour and 6-hour points. All data are presented as the mean ± SEM and each symbol corresponds to a biological replicate (*n* = 3 per group). Results are representative of three independent experiments. *P* values were calculated using one-way ANOVA with Bonferroni multiple-comparison test. **b**, Allergen-induced degranulation of the WT-FcεRI$^+$ RBL-2H3 cells. β-Hexosaminidase release in RBL-2H3 cells expressing WT-FcεRI was induced by C48/80 (positive control) and IgE/*Phl p 7* stimulation. IgE refers to 102.1F10 IgE[40,41], which responds to the *Phl p 7* allergen. IgE responds to the antigen gp120. All data are presented as the mean ± SEM and each symbol corresponds to a biological replicate (*n* = 3 per group). Results are representative of three independent experiments. *P* values were calculated using one-way ANOVA with Bonferroni multiple-comparison test.

Extended Data Table 1 | Statistics of the cryo-EM analysis on human FcεRI and its complex with IgE

	FcεRI complex (EMD-39614) (PDB 8YVU)	IgE/FcεRI complex (EMD-39627) (PDB 8YWA)
Data collection and processing		
Magnification	81,000	81,000
Voltage (kV)	300	300
Electron dose (e-/Å^2)	50	50
Defocus range (μm)	-1.0 to -1.8	-1.0 to -1.8
Pixel size (Å)	1.087	1.087
Symmetry imposed	C1	C1
Initial particles images (no.)	75,503,491	60,805,461
Final particles images (no.)	239,131	920,752
Map resolution (Å)	3.74	3.14
FSC threshold	0.143	0.143
Map resolution range (Å)	3.6-5.0	2.5-5.0
Refinement		
Initial model used (PDB code)		8C1C
Map resolution (Å)	4.0	3.8
FSC threshold	0.5	0.5
Map sharpening B-factor (Å^2)	-201.6	-153.7
Model composition		
Protein residues	514	1470
B factors (Å^2)		
Protein	115.3	68.59
R.m.s deviations		
Bonds length (Å)	0.003	0.004
Bonds Angle (°)	0.627	0.488
Validation		
MolProbity score	1.78	1.92
Clashscore	8.64	8.65
Poor rotamers (%)	0.22	0.55
Ramachandran plot		
Favored (%)	95.53	94.07
Allowed (%)	4.09	5.79
Disallowed (%)	0.39	0.14

Cryo-EM density maps and structural coordinates have been deposited in the Electron Microscopy Data Bank (EMDB) and Protein Data Bank (PDB), respectively and the corresponding accession codes are shown in the table.

nature portfolio

Corresponding author(s): Qiang Su, Yigong Shi

Last updated by author(s): Sep 30, 2024

Reporting Summary

Nature Portfolio wishes to improve the reproducibility of the work that we publish. This form provides structure for consistency and transparency in reporting. For further information on Nature Portfolio policies, see our Editorial Policies and the Editorial Policy Checklist.

Statistics

For all statistical analyses, confirm that the following items are present in the figure legend, table legend, main text, or Methods section.

n/a	Confirmed	
☐	☒	The exact sample size (*n*) for each experimental group/condition, given as a discrete number and unit of measurement
☐	☒	A statement on whether measurements were taken from distinct samples or whether the same sample was measured repeatedly
☐	☒	The statistical test(s) used AND whether they are one- or two-sided *Only common tests should be described solely by name; describe more complex techniques in the Methods section.*
☒	☐	A description of all covariates tested
☒	☐	A description of any assumptions or corrections, such as tests of normality and adjustment for multiple comparisons
☐	☒	A full description of the statistical parameters including central tendency (e.g. means) or other basic estimates (e.g. regression coefficient) AND variation (e.g. standard deviation) or associated estimates of uncertainty (e.g. confidence intervals)
☐	☒	For null hypothesis testing, the test statistic (e.g. *F*, *t*, *r*) with confidence intervals, effect sizes, degrees of freedom and *P* value noted *Give P values as exact values whenever suitable.*
☒	☐	For Bayesian analysis, information on the choice of priors and Markov chain Monte Carlo settings
☒	☐	For hierarchical and complex designs, identification of the appropriate level for tests and full reporting of outcomes
☒	☐	Estimates of effect sizes (e.g. Cohen's *d*, Pearson's *r*), indicating how they were calculated

Our web collection on statistics for biologists contains articles on many of the points above.

Software and code

Policy information about availability of computer code

Data collection	EPU 2
Data analysis	Coot 0.8.9.1, Chimera 1.15, cryoSPARC v4, ChimeraX 1.6.1, Phenix 1.19.2, GraphPad Prism 9, FlowJo 10.8.1, LAS X 1.4.6, SEDFIT 16.1c, SEDNTERP 3, HISAT2 2.2.1, fastp v0.23.0, edgeR 3.19

For manuscripts utilizing custom algorithms or software that are central to the research but not yet described in published literature, software must be made available to editors and reviewers. We strongly encourage code deposition in a community repository (e.g. GitHub). See the Nature Portfolio guidelines for submitting code & software for further information.

Data

Policy information about availability of data

All manuscripts must include a data availability statement. This statement should provide the following information, where applicable:

- Accession codes, unique identifiers, or web links for publicly available datasets
- A description of any restrictions on data availability
- For clinical datasets or third party data, please ensure that the statement adheres to our policy

The atomic coordinates for the FcεRI dimer and the IgE/FcεRI complex have been deposited in the PDB with the accession codes 8YVU and 8YWA, respectively. The corresponding EM maps have been deposited in the EMDB with the accession codes EMD-39614 and EMD-39627. The other structural coordinates used in this study are available from PDB 8C1C and 1F6A. In the RNA-seq experiment, raw sequencing data was aligned to the rat reference genome (Rnor_6.0). The RNA-seq data generated in this project are available in GEO repository under accession numbers GEO: GSE278387.

Research involving human participants, their data, or biological material

Policy information about studies with human participants or human data. See also policy information about sex, gender (identity/presentation), and sexual orientation and race, ethnicity and racism.

Reporting on sex and gender	n/a
Reporting on race, ethnicity, or other socially relevant groupings	n/a
Population characteristics	n/a
Recruitment	n/a
Ethics oversight	n/a

Note that full information on the approval of the study protocol must also be provided in the manuscript.

Field-specific reporting

Please select the one below that is the best fit for your research. If you are not sure, read the appropriate sections before making your selection.

☒ Life sciences ☐ Behavioural & social sciences ☐ Ecological, evolutionary & environmental sciences

For a reference copy of the document with all sections, see nature.com/documents/nr-reporting-summary-flat.pdf

Life sciences study design

All studies must disclose on these points even when the disclosure is negative.

Sample size	Sample sizes for the Cryo-EM datasets were selected based on the need to achieve sufficient particle counts required for high-resolution structure determination, a well-established criterion in structural biology. For the cell-based assays, sample sizes were determined by the ability to consistently generate conclusive and reproducible results. Although no formal sample size calculations were performed, the chosen sample sizes reflect standard practices in the field and were sufficient to observe robust and statistically significant outcomes. Importantly, additional data collection did not change the conclusions of the study, indicating that the selected sample sizes were adequate to capture the biological phenomena under investigation.
Data exclusions	Data exclusions were based on predefined experimental criteria to ensure accuracy and consistency in the results. Specifically, data points were excluded if they showed technical errors, such as equipment malfunctions, or if they deviated significantly from expected experimental conditions (e.g., improper cell viability or abnormal signal readings). These exclusion criteria were pre-established to maintain the integrity and reliability of the dataset, ensuring that only valid and reproducible data contributed to the final analysis.
Replication	Experiment was repeated at least twice and the results were successfully reproduced. The number of biological and technical replicates were indicated in the figure legends.
Randomization	For the structural studies, during the 3D refinement process, the particle images were randomly divided into two separate groups. During 2D classification, each particles assigned to a random class with a random orientation. For the cell-based assay, the cells used was allocated randomly.
Blinding	For all experiments, there are both negative and positive controls and all the results were obtained in parallel using the same setting, and each treatment was assigned to a number during the experiment.

Reporting for specific materials, systems and methods

We require information from authors about some types of materials, experimental systems and methods used in many studies. Here, indicate whether each material, system or method listed is relevant to your study. If you are not sure if a list item applies to your research, read the appropriate section before selecting a response.

Materials & experimental systems

n/a	Involved in the study
☐	☒ Antibodies
☐	☒ Eukaryotic cell lines
☒	☐ Palaeontology and archaeology
☒	☐ Animals and other organisms
☒	☐ Clinical data
☒	☐ Dual use research of concern
☒	☐ Plants

Methods

n/a	Involved in the study
☒	☐ ChIP-seq
☐	☒ Flow cytometry
☒	☐ MRI-based neuroimaging

Antibodies

Antibodies used	Primary antibodies: FcεRIα (Cat: DF6593, Affinity Biosciences, Polyclonal). Secondary antibodies:Goat Anti-Mouse IgG (Cat: CW0102, CWBIO); Goat Anti-Rabbit IgG (H+L) HRP (Cat: S0001, Affinity Biosciences). Flow cytometry antibodies: FITC anti-human FcεRIα (Cat: 334607, Biolegend).
Validation	All antibodies are commercially available and validated by the manufacturer to demonstrate its ability to detect corresponding target. None were independently validated by us. For FcεRIα (Cat: DF6593, Affinity Biosciences, Polyclonal), the specificity is that FcεRIα Antibody detects endogenous levels of total FcεRIα. For FITC anti-human FcεRIα (Cat: 334607, Biolegend), the antibody has been reported to bind the receptor even in the presence of IgE.

Eukaryotic cell lines

Policy information about cell lines and Sex and Gender in Research

Cell line source(s)	The ExpiHEK293F cell was purchased from Thermo Fisher Scientific Inc.; (Code No. A14527CN). Lenti-X 293T was from TaKaRa (Clontech; Code No.632180). The human LAD2 cells were from Jian-Hua Wang Lab at Chinese Academy of Sciences (Guangzhou). The LAD2 cells were originally come from Cellosaurus LAD 2 (CVCL_0387). The parental RBL-2H3 cell was purchased from Company. Stable cell lines of RBL-2H3 cell were generated and validated in house.
Authentication	RBL-2H3 cell lines were checked for FcεRI expression by staining with FITC anti-human FcεRIα. The Lenti-X 293T, ExpiHEK293F, and LAD2 cell lines were not authenticated.
Mycoplasma contamination	In this study, except for RBL-2H3 cell line, no mycoplasma contamination was detected in other cell lines, and the parent RBL-2H3 cell line was checked and detected without mycoplasma contamination before delivery
Commonly misidentified lines (See ICLAC register)	There is no commonly misidentified cell lines used in this study.

Flow Cytometry

Plots

Confirm that:

☒ The axis labels state the marker and fluorochrome used (e.g. CD4-FITC).

☒ The axis scales are clearly visible. Include numbers along axes only for bottom left plot of group (a 'group' is an analysis of identical markers).

☒ All plots are contour plots with outliers or pseudocolor plots.

☒ A numerical value for number of cells or percentage (with statistics) is provided.

Methodology

Sample preparation	RBL-2H3 cells expressing different FcεRI variants were harvested and washed twice in fluorescence-activated cell sorting (FACS) buffer consisting of phosphate-buffered saline (PBS) supplemented with 2% (v/v) fetal bovine serum (FBS). The cells were then incubated with anti-human FcεRIα-FITC (Biolegend) at a dilution of 1:500 for 30 minutes on ice, followed by washing twice using the FACS buffer (PBS supplemented with 2% (v/v) FBS) before flow cytometry analysis. For the analysis of IgE staining, RBL-2H3 cells expressing different FcεRI variants were suspended in 200 µL FACS buffer, incubated with IgE-moxBFP at final concentration of 0, 5, 10, 25, 50 µg/mL at 25°C for 30 minutes.
Instrument	Samples were acquired on Cyto-FLEX LX -5L2 (Beckman).
Software	Resulting data was analyzed in FlowJo (version 10.8.1; Treestar & BD Biosciences).
Cell population abundance	Cells were expanded as described before they were analyzed after sorting.

Gating strategy	IgE binding assays: FSC-A/SSC-A > Singlets using FSC-A/FSC-H > moxBFP positive/mCherry positive cells surface expression FcεRIα: FSC-A/SSC-A > Singlets using FSC-A/FSC-H > mCherry positive cells > FcεRIα-FITC positive cells

☒ Tick this box to confirm that a figure exemplifying the gating strategy is provided in the Supplementary Information.